Hydrothermal Synthesis and Characterization of $BaTiO_3$ Nanopowders with and without Reduced Graphene Oxide (rGO)

Name: Muhammad Farhan Mehmood
Reg No: 2010-NUST-MS PhD-MS-E-09

This work is submitted as a MS thesis in partial fulfillment of the requirement for the degree of

(MS in Materials and Surface Engineering)

Supervisor: Dr. Amir Habib

School of Chemical and Materials Engineering (SCME)
National University of Sciences and Technology (NUST)
H-12, Islamabad, Pakistan.
September, 2014

Al-QURAN

"It is only those who have knowledge among

His servants that fear ALLAH. "

(35:28)

Al-HADITH

"Whoever follows a path in the pursuit of knowledge,
Allah will make a path to Paradise easy for him."
(Al-Bukhaari)

Certificate

This is to certify that work in this thesis has been carried out by **Muhammad Farhan Mehmood** and completed under my supervision in Nanomaterials Synthesis Laboratory, School of Chemical and Materials Engineering, National University of Sciences and Technology, H-12, Islamabad, Pakistan.

Co-supervisor _____

Dr. Iftikhar H. Gul
Assistant Professor
Materials Engineering Department
National University of Sciences & Technology, Islamabad

Supervisor _____

Dr. Amir Habib
Assistant Professor
Materials Engineering Department
National University of Sciences & Technology, Islamabad

Submitted through

Prof. Dr. Mohammad Mujahid
Principal/Dean,
School of Chemical and Materials Engineering
National University of Sciences and Technology, Islamabad

DEDICATION

To my beloved parent, sister and brothers who have prayed for my glorious future and have demand nothing for their endless efforts

ACKNOWLEDGEMENT

First of all, I am grateful to **Almighty ALLAH**, The Light of Heavens and Earth. The One Who helped me in my whole life and does mercy on me to reach this position and helped me to complete this project. As without His help I can't do anything. Peace and blessings of the Allah be upon the Holy Prophet, **Hazrat Muhammad (S.A.W.W)**, who exhorted his followers to seek for knowledge from cradle to grave.

With great respect, sincere thanks and heart felt obligations to **Dr. Muhammad Mujahid,** Principal SCME NUST and **Dr. Muhammad Shahid,** Head of Department, SCME NUST and all my teachers whose efforts embellished me with courage and confidence and who in one way or the other enlightened me to reach this stage.

I thanks my supervisor, **Dr. Amir Habib,** Assistant Professor SCME, NUST, Islamabad for his exceptional academic and scientific guidance during my M.S study. I really appreciate his constant encouragement throughout my project, his faith in the abilities of the students and his ready availability on all matters.

It is indeed an honor for me for expressing my heartiest gratitude to my Co-supervisor **Dr. Iftikhar H. Gul** for his constructive suggestions in my M.S research and dissertation. His help regarding technical guidance, encouragement and moral aspects is really acknowledgeable and appreciated.

Lastly, but no means in the least, I would like to thanks and acknowledged the backbone of my research, my family especially, their continuous support, positive attitude and prays really encourage and belief in me toward success. Words fail to express the intensity of gratitude to my great father and loving mother who have devoted their lives and sacrifice their comforts for my studies and guidance. Moreover, I am deeply indebted to my most loving brothers, sidter and all other relatives who remembered me in their prayers. May Almighty Allah bless them always (Ameen). Better to put full stop here.

Muhammad Farhan Mehmood

ABSTRACT

The main purpose of present study is to synthesis nano-sized $BaTiO_3$ powders using $Ba(OH)_2$ and TiO_2 by stirred reactor hydrothermal process with and without rGO (reduced Graphene Oxide). $BaTiO_3$ powders are prepared at various reaction temperature and time in the presence or wihtout rGO already obtained via chemical exfoliation. X-ray diffraction, Raman spectroscopy, Impedence and scanning electron microscopy (SEM) are used to characterize the synthesized $BaTiO_3$ powders. XRD and Raman spectroscopy data revealed that cubic phase nano-sized $BaTiO_3$ powders are successfully obtained in all the cases. In case of BT without rGO at elevated temperature 160°C revealed the presence of tetragonal phase while at the same temperature with rGO obtained BT has the cubic phase with well defined morphology and crystallanity. Hence the presence of rGO restricted the BT to its cubic phase while the crystallanity and morphology improved with exact stichiometry.

CONTENTS

CHAPTER 1

1 Overview of Hydrothermal Materials Synthesis Technology

CHAPTER 2

2 Review of Hydrothermal Synthesis of $BaTiO_3$ Powders

CHAPTER 3

3 Materials and Methods

CHAPTER 4

4 Result and Discussion

List of Figures

CHAPTER 1

OVERVIEW OF HYDROTHERMAL MATERIALS SYNTHESIS TECHNOLOGY

1.1. INTRODUCTION

Hydrothermal synthesis is a process that utilizes single or heterogeneous phase reactions in aqueous media at elevated temperature (T>25°C) and pressure (P>100 kPa) to crystallize ceramic materials directly from solution. The synthesis process is typically carried out in a pressurized vessel called an autoclave with the reaction in aqueous solution. The temperature in the autoclave can be raised above the boiling point of water, reaching the pressure of vapor saturation. Definition for the word hydrothermal has undergone several changes from the original Greek meaning of the words 'hydros' meaning water and 'thermos' meaning heat. Recently, hydrothermal process has been defined as "*any heterogeneous chemical reaction takes place in the presence of a solvent (whether aqueous or non-aqueous) above the room temperature and at pressure greater than 1 atm in a closed system*".

The term 'hydrothermal' is purely of geological origin. It was first used by the British geologist, Sir Roderick Murchison (1792-1871) to describe the action of water at elevated temperature and pressure, in bringing about changes in the earth's crust leading to the formation of various rocks and minerals. Hydrothermal research was initiated in the middle of 19^{th} century by geologists and was aimed at laboratory simulations of natural hydrothermal phenomena. In the 20^{th} century, hydrothermal synthesis was clearly identified as an important technology for materials synthesis, predominantly in the fields of hydrometallurgy and single crystal growth [1]. In recent years, commercial interest in hydrothermal synthesis has been revived in part because a steadily increasing large family of materials, primarily ceramic powders, has emerged that can be prepared under mild conditions (T<350ºC, P<100 MPa). The growing number of scientific research papers, which almost tripled between 1989 and 2005, illustrates the rising interest in hydrothermal synthesis. During this period, USA, Japan, and China contributed 70% of all the research papers on hydrothermal processing in materials science published in the

world, with the China (44%) leading ahead of Japan (15%) and USA (11%) [2]. The rising interest on hydrothermal synthesis of ceramic powders is illustrated in Figure 1.1.

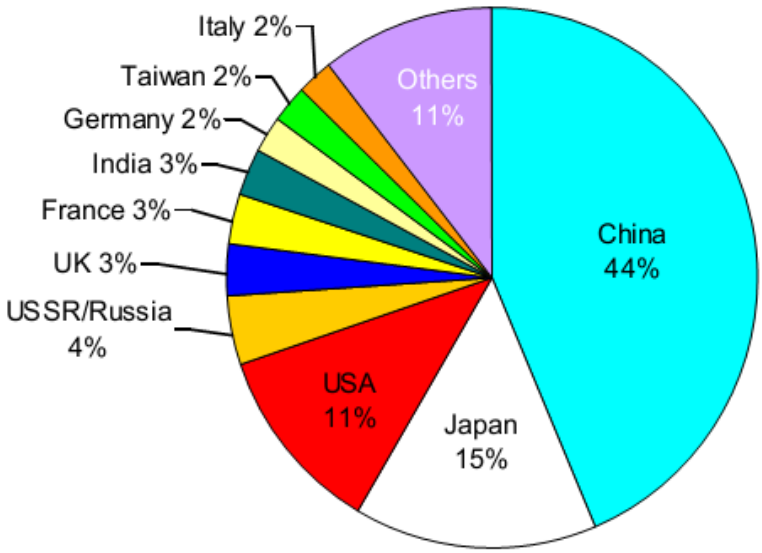

Figure 1.1: Geographical distribution of the research on hydrothermal processing of ceramic powders (1989-2005) based on information available in Science Citation Index, Chemical Abstracts, and INSPEC databases [2].

The hydrothermal technique is ideal for the processing of very fine powders having high purity, controlled stoichiometry, high quality, narrow particle size distribution, controlled morphology, uniformity, less defects, dense particles, high crystallinity, excellent reproducibility, controlled microstructure, high reactivity with ease of sintering etc. Further, this technique facilitates issues like energy saving, the use of larger volume equipment, better nucleation control, avoidance of pollution, higher dispersion, higher rates of reaction, better shape control, and lower temperature operations in the presence of the solvent.

In nanotechnology, the hydrothermal technique has an edge over other materials processing techniques, since it is ideal for the processing of designer particulates as shown in Figure 1.2.

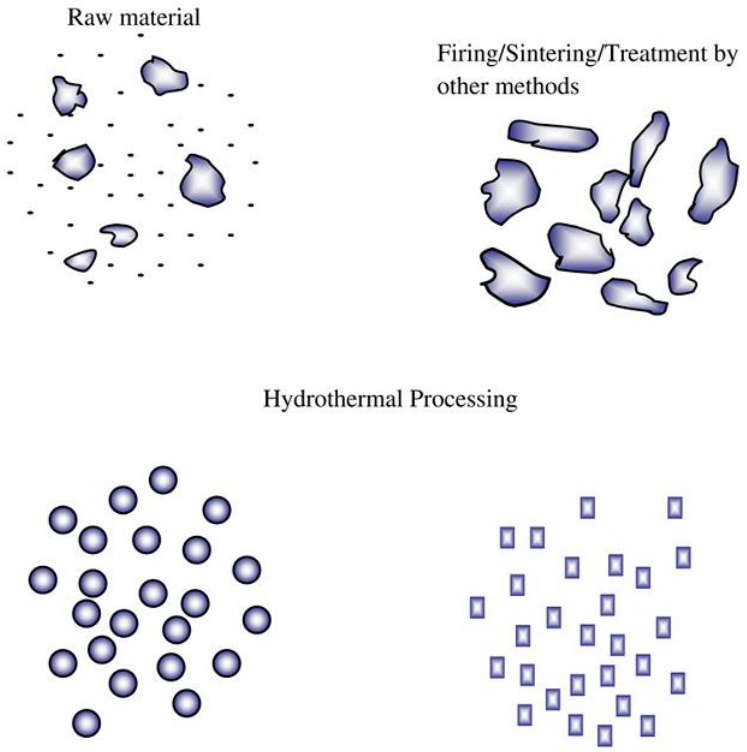

Figure 1.2: Difference in particle processing by hydrothermal and conventional techniques [3].

The hydrothermal technique is becoming one of the most important tools for advanced materials processing, particularly owing to its advantages in the processing of nanostructured materials for a wide variety of technological applications such as electronics, optoelectronics, catalysis, ceramics, magnetic data storage, biomedical, biophotonics, etc. This technique not only helps in processing monodispersed and highly homogeneous nanoparticles, but also acts as one of the most attractive techniques for processing nano-hybrid and nano-composite materials. Syntheses are usually conducted at autogenous pressure, which corresponds to saturated vapor pressure of the solution at specified temperature and composition of hydrothermal solution. Upper limits of hydrothermal synthesis extend to over 1000 ºC and 500 MPa pressures [4]. However, mild conditions are preferred for commercial processes where temperatures are less than 350 ºC and pressures less than approximately 50 MPa. Intensive research has led to a

better understanding of hydrothermal chemistry, which has significantly reduced the reaction time, temperature, and pressure for hydrothermal crystallization of materials (T<200ºC, P<1.5 MPa) [1-5]. This breakthrough has made hydrothermal synthesis more economical since processes can be engineered using cost-effective and proven pressure reactor technology and methodologies already established by the chemical process industry.

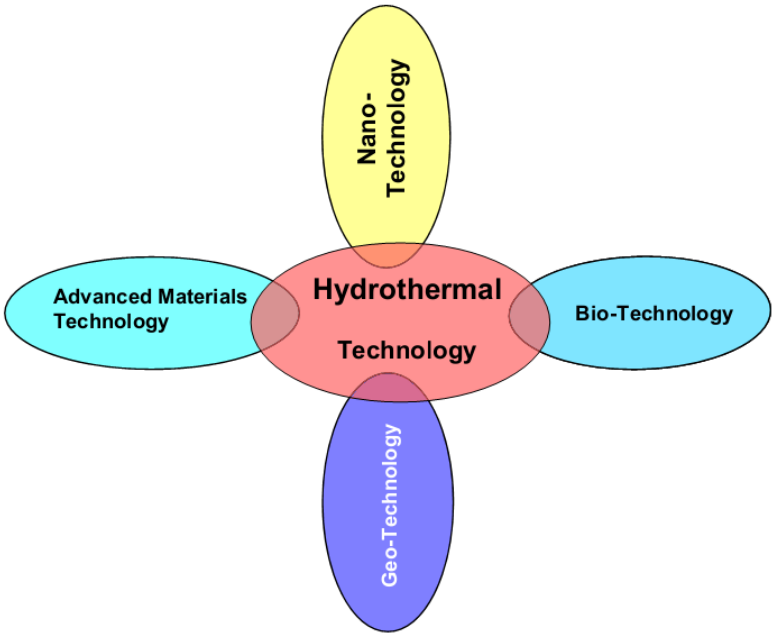

Figure 1.3: Hydrothermal technology in the 21st century [5].

Hydrothermal technology in the 21st century is not just confined to the crystal growth or leaching of metals, but it is growing to take a very broad shape covering several interdisciplinary branches of science like geotechnology, biotechnology, nanotechnology and advanced materials technology as illustrated in Figure 1.3 [5]. So, the hydrothermal processing of advanced materials is a highly interdisciplinary subject and the technique is being used by physicists, chemists, ceramists, hydrometallurgists, materials scientists, engineers, biologists, geologists and technologists etc. It has now

emerged as a frontline technology for the processing of advanced materials for nanotechnology. Hydrothermal synthesis can be distinguished from solvothermal synthesis methods [6-7] and soft solution processing [8]. Solvothermal synthesis utilizes non-aqueous solvents instead of an aqueous medium [9]. For example, glycothermal synthesis is a solvothermal method that utilizes glycols solvents such as ethylene glycol or 1,4-butanediol. Soft solution processing is a broad term that encompasses many well-established, processing routes that utilize mild reaction conditions, which include hydrothermal synthesis among other methods such as bio-mimetic processing, electro-deposition, self-assembly, etc.

The hydrothermal synthesis technology can be hybridized microwaves, electrochemistry, ultrasound, mechanochemistry, optical radiation, hot-pressing, and many other processes to enhance reaction kinetics as well to make new materials.

1.1.1. Microwave hydrothermal synthesis process:

This process is used mostly for synthesis of ceramic powders. It enhances crystallization kinetics by l-2 orders of magnitude with respect to standard hydrothermal processing [10]. Additional advantages of this method are very high heating rates and the synthesis of novel phases. The hydrothermal-microwave technique has been used to synthesize different ceramic powders with controlled size and morphology, such as TiO_2, ZrO_2, Fe_2O_3, $BaTiO_3$, hydroxyapatite, etc. [10-11].

1.1.2. Hydrothermal electrochemical synthesis process:

This process combines the hydrothermal method with electrochemical treatment and involves deposition of polycrystalline oxide films on reactive metal electrode substrates. It is particularly important when crystalline oxide products cannot precipitate from solution in the absence of an applied electrical potential. Highly crystallized ceramic thin films, such as $BaTiO_3$, $SrTiO_3$, $LiNiO_2$, $PbTiO_3$, $CaWO_4$, and $BaMoO_4$ can be deposited on metallic substrates from aqueous solutions at low temperatures 25-200°C within several hours by the hydrothermal-electrochemical method [12-13]. The hydrothermal-electrochemical technique also enables fabrication of ceramic superlattices. Alternate layers of thallium (RI) oxide films (7 nm thick) with different defect structures were deposited using this method [14]. Monomolecular layers of semiconductors, such as GaAs, CdTe, CdSe, and CdS are made by electrochemical

atomic layer epitaxy, which is analogous to molecular beam epitaxy, but instead uses aqueous solutions instead of a vapor phase for transport of growth species [15-16].

1.1.3. Mechanochemical hydrothermal synthesis process:

This process also called as "wet mechanochemical" hybridizes hydrothermal synthesis and the classical mechanochemical powder synthesis, which is a solid-state synthesis method that takes advantage of the perturbation of surface-bonded species by pressure to enhance thermodynamic and kinetic reactions between solids [17]. Materials such as $PbTiO_3$ and hydroxyapatite have been made with this approach [17-18]. It is known that high pressures in excess of 1GPa catalyze low-temperature solid-state reactions in ceramic materials by orders of magnitude [19]. The synthesis process utilizes the solvency of an aqueous solution, which capitalizes on using the pressure environment provided by the mechanochemical reactor to accelerate one or more the rate-determining steps that limit the lower temperature for hydrothermal reactions such as interfacial reaction, crystal dissolution or dehydroxylation.

The mechanochemical activation of slurries can generate localized zones of high temperature (~450-700 °C) and high pressure due to friction and adiabatic heating of gas bubbles (if present in the slung), while maintaining the average temperature close to the room temperature [20]. Since any type of mill or comminuting equipment can be used, the mechanochemical-hydrothermal route offers the potential for process scale-up yet eliminates the need for use of a pressure vessel or external heating. However, control of particle size, morphology and aggregation is a challenge for this method since current methods fail to regulate rates of nucleation, growth and aging, as well as conventional hydrothermal technologies are able to. To address this issue, recent work [21] has incorporated the use of emulsions in mechanochemical-hydrothermal reactors to better regulate nucleation and growth, which resulted in hydroxyapatite that is far less aggregated.

1.1.4. Hydrothermal sonochemical synthesis process:

This process hybridizes hydrothermal synthesis with ultrasound (acoustic 20 kHz-10MHz). Ultrasound is known to accelerate the reaction kinetics by as much as two orders of magnitude [19]. This has been attributed to sharp temperature gradients with localized peak temperature zones that are speculated to be as high as 5000 K and

localized peak pressure zones of up to 180 MPa, while maintaining the average temperature close to room temperature [22]. These gradients create CaviationI bubble collapse events that inhibit the formation of agglomerates or aggregates during crystallization. The sonochemical environment is also considered to alter molecular chemistry (chemical bond scission, generate excited states and accelerate electron transfer steps in chemical reactions), and enhance mass transport and crystallization kinetics [44]. Hydrothermal-sonochemical synthesis methods have been reported for many ceramic powders ($Ca_{10}(PO_4)_6(OH)_2$, $AlPO_4$, InSb, CdS) and thin films ($Li_2B_4O_7$, $Ba_2TiSi_2O_8$).

1.1.5. Hydrothermal photochemical synthesis process:

Hydrothermal photochemical synthesis process utilizes laser irradiation is to increase growth rates by an order of magnitude for ceramics and 3 orders of magnitude for metals [23-24]. It enables precise patterning of thin films with a resolution of ~1μm, which is essential in the integration of hydrothermal techniques with other device fabrication technologies. Enhancement of the reaction rate can be attributed to temperature, diffusional enhancement due to light-induced thermal-gradients that micro-stir the solution and/or photochemistry [25]. Examples of ceramics synthesized by the hydrothermal-photochemical include thin films of Ni-, Zn-, Co-, and Mn-ferrites, Co_3O_4, Tl_2O_3, and Fe_3O_4.

1.1.6. Hydrothermal hot pressing synthesis process:

This is a simple and effective fabrication technique for shaped ceramics under mild conditions (T= l00-350 °C, P>25 MPa), within a short reaction time below 1 h, often in only one processing step (reactive hydrothermal sintering or hot pressing). This technique is very useful for solidification of radioactive wastes and sludge ashes [26]. The process involves compacting of a ceramic powder or its precursor under hydrothermal conditions either in a special hot-pressing apparatus where uniaxial pressure can be applied or simply in a metal capsule [27-28]. Another possibility is direct hydrothermal sintering of a pressed pellet of powder. During the process, mass transport leading to densification occurs mostly by a dissolution-precipitation mechanism. The resulting materials are usually very porous, but exhibit fairly good mechanical properties. Nevertheless, relative densities as high as 94% have been reported [28]. Low processing

temperatures enable the incorporation of organic components that can improve mechanical strength of the porous ceramics. Examples of ceramics synthesized and/or densified by this method include zirconia, titania, silica, calcium carbonate, strontium carbonate, magnesium carbonate, hydroxyapatite, glass, and mica.

1.2. Advantages of Hydrothermal Synthesis:

Hydrothermal synthesis offers many advantages over conventional and non-conventional ceramic synthetic methods. All forms of ceramics can be prepared with hydrothermal synthesis, namely powders, fibers, and single crystals, monolithic ceramic bodies, and coatings on metals, polymers, and ceramics. Some main advantages of hydrothermal process are [29-31]:

- Production of pure and fine particles with a narrow size distribution
- Production of spherical morphology particles
- Direct preparation of crystalline powders without high-temperature calcination
- Synthesized powders do not need milling step before sintering, thus avoiding contamination
- Powders are highly reactive during sintering

1.3. Aim of the Work: Hydrothermal/ solvothermal synthesis of $BaTiO_3$ powders:

Traditionally $BaTiO_3$ are produced via the mixed route, consisting of repeated ball-milling and solid-state reaction of $BaCO_3$ and TiO_2 powder mixture at temperature around 1027 °C [32-33]. This method leads to the production of $BaTiO_3$ particles of irregular and uncontrolled morphologies, which limit the electrical properties of the product. Recently, most studies have been focused on low-temperature synthesis and particle morphology control of $BaTiO_3$ with sol–gel processing [34], the oxalate route [35], microwave heating [36] and micro-emulsion process [37] have been developed to improve the homogeneity and purity of $BaTiO_3$ powders. However, the products obtained from these solution-based techniques are either amorphous or impure representing precursor compounds, so that needs calcination step at 700 °C followed by milling to remove unreacted organic compounds to form a pure crystalline phase. Thus a significant improvement in the powder quality is normally not achieved because the calcination and milling steps are similar to those used in the solid-state method.

Furthermore, metal alkoxides used in sol-gel processes are generally too expensive for practical applications. Therefore, methods for cost-effective production of pure, ultra-fine nanocrystalline $BaTiO_3$ particles with spherical morphology and narrow particle-size distribution are to be developed. Among these syntheses routes, the hydrothermal synthesis brings about some advantages on the preparation of fine and homogeneous powders with high-purity single and multi-component oxides [38-39].

The main purpose of present study is to synthesize high purity $BaTiO_3$ powders using hydrothermal/solvothermal method. The influences of reaction temperatures and time on the crystal morphology of $BaTiO_3$ powders are carried out.

1.4. Objectives:

Following are the main objectives of the present research project:

- Hydrothermal synthesis of $BaTiO_3$ powders at varied temperatures (100-180 °C) and reaction times (1-8 hr)
- Characterization of synthesized $BaTiO_3$ powders using various state-of-the-art techniques viz., x-ray diffraction (XRD), scanning electron microscopy (SEM), Raman Spectroscopy, Fourier transform infra-red (FTIR) spectroscopy and Impedance spectroscopy

CHAPTER 2

REVIEW OF HYDROTHERMAL SYNTHESIS OF BARIUM TITANATE ($BaTiO_3$) POWDERS

2.1. Barium titanate ($BaTiO_3$):

Barium titanate is an oxide of barium (Ba) and titanium (Ti) with the chemical formula $BaTiO_3$. It is a white powder and transparent as larger crystals having density 6.02 g/cm^3 and melting point 1625 °C). Like many oxides, barium titanate is insoluble in water but attacked by sulfuric acid (H_2SO_4). Its bulk room-temperature band gap is 3.2 eV, but it increases to ~3.5 eV when the particle size is reduced from about 15 to 7 nm.

Barium titanate ($BaTiO_3$), a pervoskite structure material, has been one of the best known and widely used ferroelectric materials for because of its excellent dielectric, piezoelectric, pyroelectric and ferroelectric properties. It is mainly used in the manufacturing of electronic components such as multilayer ceramic capacitors (MLCCs), sensors and actuators, and electro-optic devices, thermistors, integral capacitors in printed circuit boards (PCBs), temperature-humidity gas sensors, communication filters, memory applications, etc. [1-3].

Barium titanate powders are used as nanofillers in Poly(methylmethacrylate) (PMMA) for fabrication of thin high-k gate dielectric films for organic field effect transistors [40]. Because of people's demands, dielectric (essentially nonconducting) characteristics of ceramics materials are increasing rapidly. At the same time people are attempting to reduce the size of all communication devices as small and as light as possible. Due to this trend, high dielectric constant materials such as barium titanate nowadays become more and more important in ceramics materials.

2.1.1. Structure of $BaTiO_3$

The perovskite-like structure, named after the $CaTiO_3$ perovskite mineral [41], is a ternary compound of formula ABO_3 that A and B cations differ in size. It is considered an FCC-derivative structure in which the larger A cation and oxygen together form an FCC lattice while the smaller B cation occupies the octahedral interstitial sites in the

FCC array. There is only the oxygen being B cation's nearest neighbor. The structure is a network of corner-linked oxygen octahedral, with the smaller cation filling the octahedral holes and the large cation filling the dodecahedral holes. The unit cell of perovskite cubic structure is shown below in Figure 2.1.

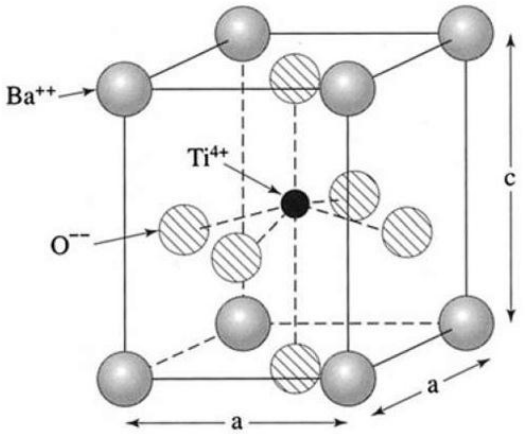

Figure 2.1: Perovskite Structure of $BaTiO_3$ [41].

In Figure 2.1., the coordination number of A (Ba^{+2}) is 12, while the coordination number of B (Ti^{+4}) is 6. In most cases, the above figure is somewhat idealized [42]. In fact, any structure consisting of the corner-linked oxygen octahedral with a small cation filling the octahedral hole and a large cation (if present) filling the dodecahedral hole is usually regarded as a perovskite, even if the oxygen octahedral is slightly distorted [43]. Also, it is unnecessary that the anion is oxygen. For example, fluoride, chloride, carbide, nitride, hydride and sulfide perovskites are also classified as the perovskite structures. As a result, the perovskite structure has a wide range of substitution of cations A and B, as well as the anions, but remembers that the principles of substitution must maintain charge balance and keep sizes within the range for particular coordination number. Because the variation of ionic size and small displacements of atoms lead to the distortion of the structure and the reduction of symmetry have profound effects on physical properties, perovskite structure materials play such an important role in dielectric ceramic. The high temperature cubic phase is easiest to describe, consisting of

octahedral TiO_6 centers that define a cube with Ti vertices and Ti-O-Ti edges. In the cubic phase, Ba^{2+} is located at the center of the cube, with a nominal coordination number of 12. Lower symmetry phases are stabilized at lower temperatures, associated with the movement of the Ba^{2+} to off-center position. The remarkable properties of this material arise from the cooperative behavior of the Ba^{2+}centres.

$BaTiO_3$ is a polymorph which exists in five phases, listing from high temperature to low temperature: hexagonal, cubic, tetragonal, orthorhombic, and rhombohedral crystal structure (Figure 2.2). All of the phases exhibit the ferroelectric effect except the cubic phase.

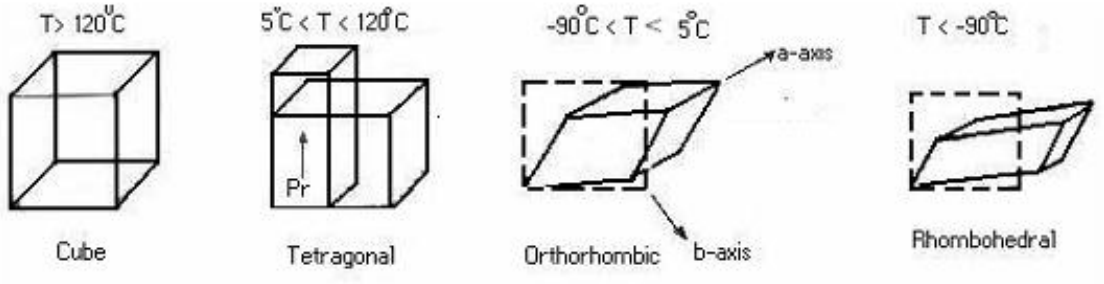

Figure 2.2: Crystallographic changes of $BaTiO_3$ [44].

Because of the practical temperature ranges, the tetragonal phase and the tetragonal to cubic phase transition region are important. The tetragonal to cubic transition temperature is usually called a Curie point. The Curie point is generally located between 120 ˚C and 130 ˚C. In the temperature range for the cubic phase, i.e., above the Curie point, the ideal perovskite structure of a cubic and symmetrical unit cell is stable. Between 0 ˚C and 130 ˚C, $BaTiO_3$ shows a distorted perovskite structure in which the Ti^{4+} and O^{-2} ions are displaced in the opposite direction from their original positions, whereas the barium ion does not change its position. This result in a large change of the Ti-O bond length compared to a small change in the Ba-O bond during the cubic to tetragonal phase changes [27]. A perovskite lattice structure, the displacement of

the Ti^{4+} and O^{2-} ions and the slight distortion of oxygen octahedral during the cubic to tetragonal phase transition are shown in Figure 2.3.

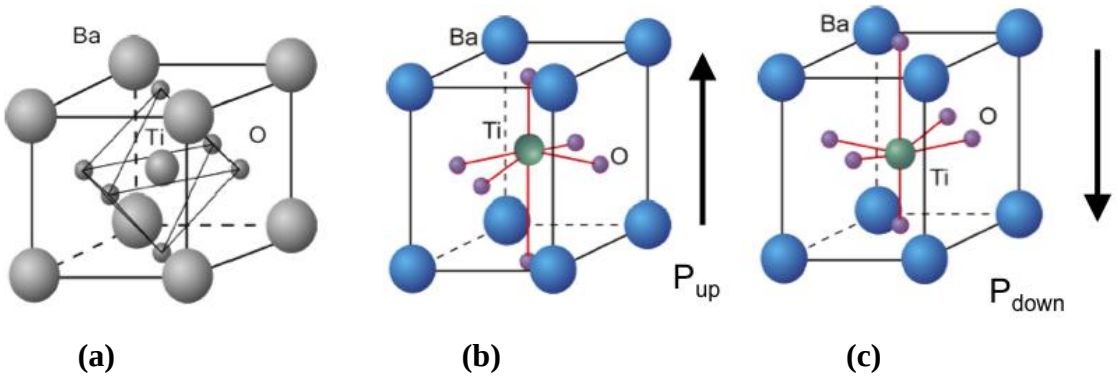

Figure 2.3: (a) Perovskite structure of $BaTiO_3$ above Curie point, (b) a-axis projection of tetragonal $BaTiO_3$ with atomic displacements, and (c) change in lattice along c-axis [45].

These ionic displacements also result in a change in lattice dimensions, and a negative linear thermal expansion coefficient along the c-axis, while a thermal expansion coefficient is usually positive due to a-, b-axes expansion. As shown in Figure 2.4, the crystal structure of $BaTiO_3$ becomes less and less tetragonal as the temperature increases toward the tetragonal to cubic transition temperature [46]. Cubic $BaTiO_3$ shows paraelectric properties, while tetragonal $BaTiO_3$ shows ferroelectric properties which are more interesting properties of $BaTiO_3$ for dielectric applications.

The relative dielectric constant variations along a-, b- and c-axes of the single crystalline $BaTiO_3$ are given in Figure 2.4. The dielectric constant along the c-axis is less than that along the a-axis may be due to the fact that oxygen ions in the c-axis, which is also cell polar axis, make strong ionic attractions with the center Ti^{4+} ion. This gives an interaction force between the Ti^{4+} and O^{2-} ions which makes vibration difficult because of a “pinning” effect under an external AC source.

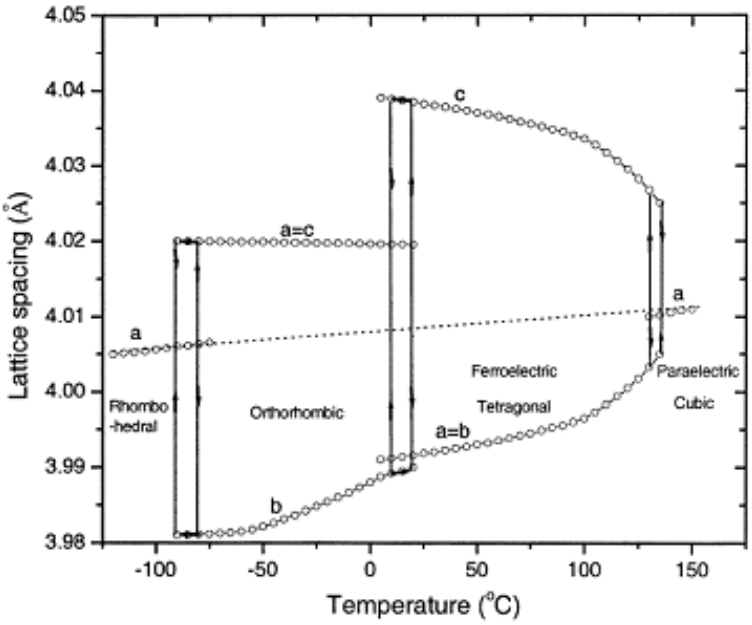

Figure 2.4: Lattice parameters of single crystal $BaTiO_3$ as a function of temperature [47].

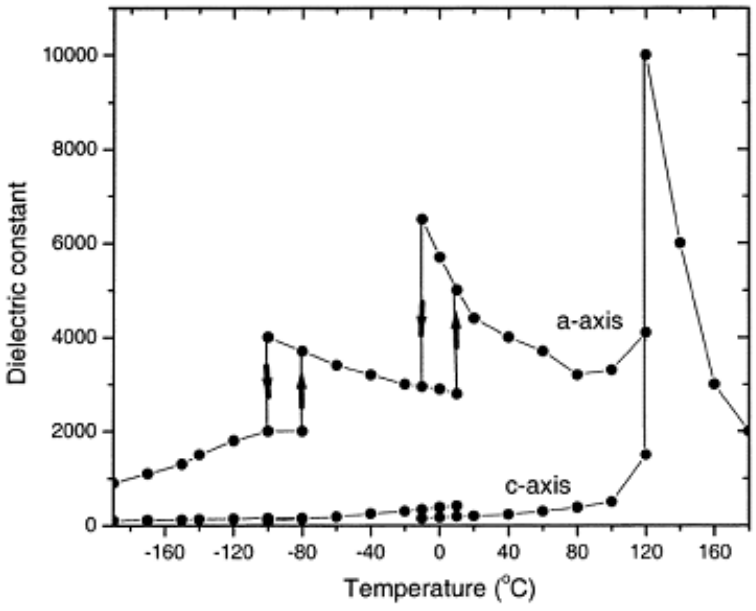

Figure 2.5: Relative dielectric constant ε_a and ε_c for single crystal $BaTiO_3$ as a function of temperature [48].

On the other hand, oxygen ions in the a- and b-axes are relatively free to vibrate perpendicularly to this c-axis; consequently, the dielectric constants along a- and b-axes are higher. In the vicinity of the Curie point, the stability of the lattice decreases and the amplitude of the vibration become higher. This induces a high dielectric constant at the Curie point. The dielectric constant of polycrystalline, non-polarized $BaTiO_3$, is an average of both curves in Figure 2.4 due to the random orientation of the individual crystals [47]. Although the basic dielectric properties of $BaTiO_3$ are well known, but the physical parameters related to the phase transition are affected by chemical purity, surface defects, particle size and sintering conditions [49-50].

2.2. Hydrothermal synthesis of $BaTiO_3$

$BaTiO_3$ powder can be successfully synthesized by solution synthesis methods using an aqueous suspension of hydrous Ti gel ($TiO_2 \cdot xH_2O$) or anhydrous TiO_2 powder and barium salts as the starting materials at temperatures ranging from 30 to 500 °C [51-57]. Recently, the introduction of titanium isopropoxide modified by addition of acetyl acetone to barium acetate in the hydrothermal synthesis leads to formation of $BaTiO_3$ at temperature as low as 50 °C [58]. Compared with other routes based on the reaction or decomposition of the solid precursors, its main superiority is an improved control method over powder homogeneity and particle uniformity. The low-temperature synthesis hydrothermal conversion of titania to barium titanate has applied the direct use of hydroxide salts, acetate salts and gels, halide salts as well as nitrate salts [59-67].

$BaTiO_3$ can be formed only in very basic conditions; TiO_2 can be obtained in less-basic media. Lencka and Riman [68-69] have developed a thermodynamic model for the calculation of phase stability in hydrothermal conditions as a function of the temperature, the precursors, the pH, and the concentrations. This model confirmed empirical results and showed a reaction yield >99.999% at high pH. Similarly, $BaTiO_3$ powders was produced [27,70] using barium hydroxide ($Ba(OH)_2$) and titanium isopropoxide in an alkoxide–hydroxide route through hydrothermal process (mixing of the precursors). Although, the powders showed good characteristics, exaggerated grain growth occurred during sintering, and high-density ceramics cannot be obtained. Although most studies involving powder synthesis focus on the mechanism of formation or on the characteristics of particles, few studies concentrate on the relationship between the synthesis conditions, the sintering ability, and the electrical properties [71-73].

To date, most of perovskite-type titanates for capacitors were made by hydrothermal method. In this case, microscopic scale $Ti(OH)_4$ gel as colloidal aggregates was used which composed of $Ti(OH)_4$ clusters with sizes from 10-50 nm. During hydrothermal synthesis, $Ti(OH)_4$ gel synthesized titanate particles had a minimum limitation in its particle size because of size in $Ti(OH)_4$ gel. Wada et al. [74] reported that minimum sizes of hydrothermal $BaTiO_3$ fine particles were limited to 20 nm. The use of Ti-chelated complex as Ti source in hydrothermal synthesis of $BaTiO_3$ fine particles, instead of $Ti(OH)_4$ gel to break this limitation. As a result, very stable Ti chelated complex with nitrilotriacetic acid (NTA) and H_2O_2 in aqueous solution was found. This Ti chelated complex was so stable, and there was no precipitate over pH of 10 and 100 °C [48]. Titanium tetrachloride ($TiCl_4$, ≥99.9% pure) was used as Ti source and H_2O_2 and nitrilotriacetic acid (NTA, $N(CH_2COOH)_3$) as chelating agents.

Barium titanate ($BaTiO_3$) powder for MLCs requires a narrow particle size distribution and a high tetragonality. However, $BaTiO_3$ powders synthesized in a hydrothermal process often exhibit lower tetragonality [45, 75] than ones produced by other wet chemical synthesis processes [76]. This in turn results in poor dielectric properties. Low tetragonality is attributed by two factors like particle size effect and hydroxyl ion effect [45]. Hydrothermal synthesized $BaTiO_3$ powders have superfine particle size, tens to hundreds of nanometers, which leads to the lattice parameter changes noted by [49]. The synthesis of mono dispersed barium titanate nanocrystals through hydrothermal recrystallization of $BaTiO_3$ nanospheres [76]. Zhu et al. have synthesized $BaTiO_3$ nanocrystals under hydrothermal conditions using titanium hydroxide and barium hydroxide as starting materials [77].

Hydrothermal synthesis of $BaTiO_3$ at 240 °C in the presence of chloride (Cl^{-1}) ions leads to the formation of tetragonal polymorph upon cooling through the Curie temperature [78]. In the absence of (Cl^{-1}) ions, the metastable cubic structure is formed. The exact role of (Cl^{-1}) ions is not clear but it leads to the formation of larger crystals (~1μm) as compared to smaller crystals (0.2 μm). In general, hydrothermal synthesis involves the reaction of $Ba(OH)_2$ and a titanium source like titanium oxide, titanium alkoxide, or titanium oxide gels. The reaction takes place in a strongly alkaline solution (~0.1 M OH^- or above), and crystalline $BaTiO_3$ is produced at temperature between 85 and 250 °C within hours.

Zhu et al. [76] synthesized $BaTiO_3$ by mixing prepared titanium hydroxide ($Ti(OH)_4$) and barium hydroxide ($Ba(OH)_2 \cdot 8H_2O$) in water and reacted in an autoclave at 100 °C for 5 hr. Similarly, they also synthesized $BaTiO_3$ nanocrystals under moderate conditions using TiO_2 and ($Ba(OH)_2 \cdot 8H_2O$) as starting materials. KOH was used as an alkaline mineralizer, and the hydrothermal reaction was carried out at 220 °C for 72 hr. in an oven. The products were washed with organic acids and deionized water for several times, and finally dried in an oven at 80-85 °C for 24 hr.

2.2.1.Titanium Precursors:

To date, most of perovskite-type titanates for capacitors were made by a hydrothermal method using various titanium precursors like anhydrous TiO_2 powder (anatase), $TiCl_4$, titanium alkoxide, or a hydrous titanium oxide gel ($TiO_2 \cdot xH_2O$), β-titanic acid (and H_2TiO_3) and tetrabutyltitanate ($Ti(C_4H_9O)_4$) etc. $Ti(OH)_4$ gel as Ti source. $Ti(OH)_4$ gel is composed of $Ti(OH)_4$ clusters with sizes from 10 to 50 nm. Thus, when hydrothermal synthesis was done, synthesized titanate particles had a minimum limitation in its particle size because of size in $Ti(OH)_4$ gel. In fact, Wada et al. reported that minimum sizes of hydrothermal $BaTiO_3$ fine particles were limited to 20 nm [74]. To break this limitation, Wada et al. proposed the use of a Ti chelated complex nitrilotriacetic acid (NTA) and H_2O_2 in aqueous solution as Ti source in hydrothermal synthesis of $BaTiO_3$ instead of $Ti(OH)_4$ gel [79]. This Ti chelated complex was so stable in aqueous solution, and there was no precipitate over pH 10 at 100 °C. Therefore, this Ti chelated complex can be used in hydrothermal synthesis of nano-sized $BaTiO_3$ particles.

2.2.2. Mechanisms of hydrothermal synthesis of $BaTiO_3$ powders:

Following two possible mechanisms have been generally proposed for hydrothermal synthesis of $BaTiO_3$ powders:

2.2.2.1. In-situ transformation mechanism:

Hertl [80] assumed and Hu et al. [65] proposed that TiO_2 particle reacts initially with dissolved barium to produce a continuous layer of $BaTiO_3$ and the additional barium must diffuse this layer and react with TiO_2 until the TiO_2 supply is exhausted. Hydrothermal reaction between nano-sized titania (TiO_2) particles and barium hydroxide ($Ba(OH)_2$) solution yields fine powders. The mechanism of nucleation and growth of $BaTiO_3$ particles have also been studied [54]. Ba^{2+} ions in the solution react with TiO_2

particle, forming a continuous $BaTiO_3$ layers on the surface of the TiO_2 particle. After that, Ba^{2+} ions diffuse through the fabricated $BaTiO_3$ layer and completely react with the TiO_2 particle. However, nano-sized particles aggregate strong because of the attractive van der Waals forces. Hence, long reaction times and high reaction temperatures are necessary to synthesize pure $BaTiO_3$ powders [81-82]. Another restriction is that nano-sized particles have a high cost as compared to sub-micron sized particles.

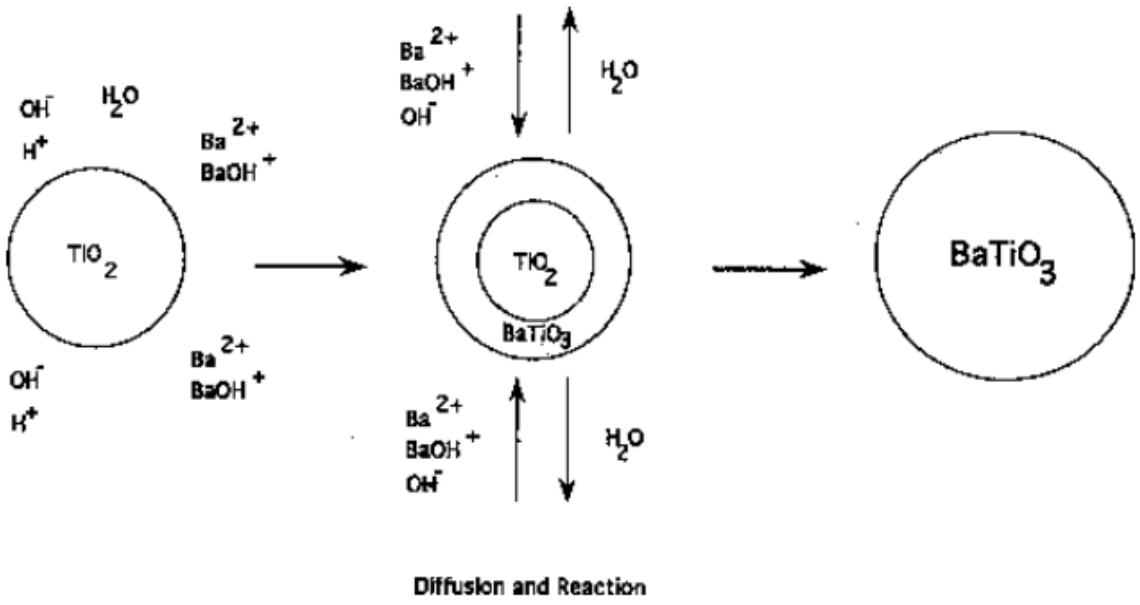

Figure 2.6: *In-situ* reaction mechanism of $BaTiO_3$ synthesis using $Ba(OH)_2$ and TiO_2 as starting materials [54].

Ball milling techniques are widely used for grinding of agglomerated powders [57, 83] and preparation of dispersed suspensions [84]. Ball milling is expected to promote the reaction of Ba^{2+} ion and TiO_2 powder. The overall conversion rate could be controlled by either diffusion rate or reaction rate. Barium titanate particles obtained through this mechanism could keep their size and morphology similar to those of the precursor titania particles. In addition, in this mechanism, two different mechanisms should be considered: the diffusion-controlled growth mechanism and the interface-controlled growth mechanism. Hu et al. [65] first synthesized mono-dispersed titania (TiO_2) powders with a diameter of 0.1–1μm and then used it as the precursor and successfully prepared $BaTiO_3$ powders by hydrothermal conversion at ≤100 °C. They

found that the size and morphology of $BaTiO_3$ particles remained the same as the precursor titania (TiO_2) particles and thought that this result agreed with the *in-situ* mechanism.

2.2.2.2. Dissolution-precipitation mechanism:

Ovramenko et al. [85] suggested and Pinceloup et al. [86] proposed that TiO_2 particle must dissolve to form hydroxy titanium complexes ($Ti(OH)^{n-}$) and then react with barium ions (Ba^{2+}) in the solution to precipitate $BaTiO_3$, which may either originate on the TiO_2 substrate or form directly in the bulk solution. Pinceloup et al. [86] studied the system of barium hydroxide–titanium tetraisopropoxide–water–isopropanol between 85 and 150 °C, and found the following results:

a) The grain size of the $BaTiO_3$ powder decreased when the solubility of the precursor decreased
b) TEM observations of incompletely reacted powder showed that the grains were either amorphous or entirely crystalline $BaTiO_3$
c) High-resolution TEM observations of fully reacted powders revealed the presence of necks between particles

They thought that these three observations provided the evidence of dissolution–precipitation mechanism. They found smaller grain sizes when the solubility of the constituents was lowered because more particles nucleating at the same time ultimately lead to finer particles. In addition, completely amorphous or completely crystalline precipitates meant no $BaTiO_3$ crystallites were found on top of the amorphous $TiO_2 \cdot xH_2O$ particles. Finally, fully reacted particles showed the presence of necks between them, which similar to those found in high temperature sintering, is more likely from a dissolution precipitation compared to an *in-situ* process.

They argue that Ba ions found near the surface of the TiO_2 particles are only temporarily adsorbed and that the composition may still be considered as $TiO_2 \cdot xH_2O$. Furthermore, if an *in-situ* mechanism is involved, the size of the particle would be very close to the initial size of the TiO_2 from which the supply of Ti derives from. This was not observed with TiO_2 nanoparticles very much smaller than the $BaTiO_3$ particles [86]. MacLaren and Ponton [87] have observed after prolonged treatment of the precipitates, $BaTiO_3$ grew within and into the amorphous TiO_2.

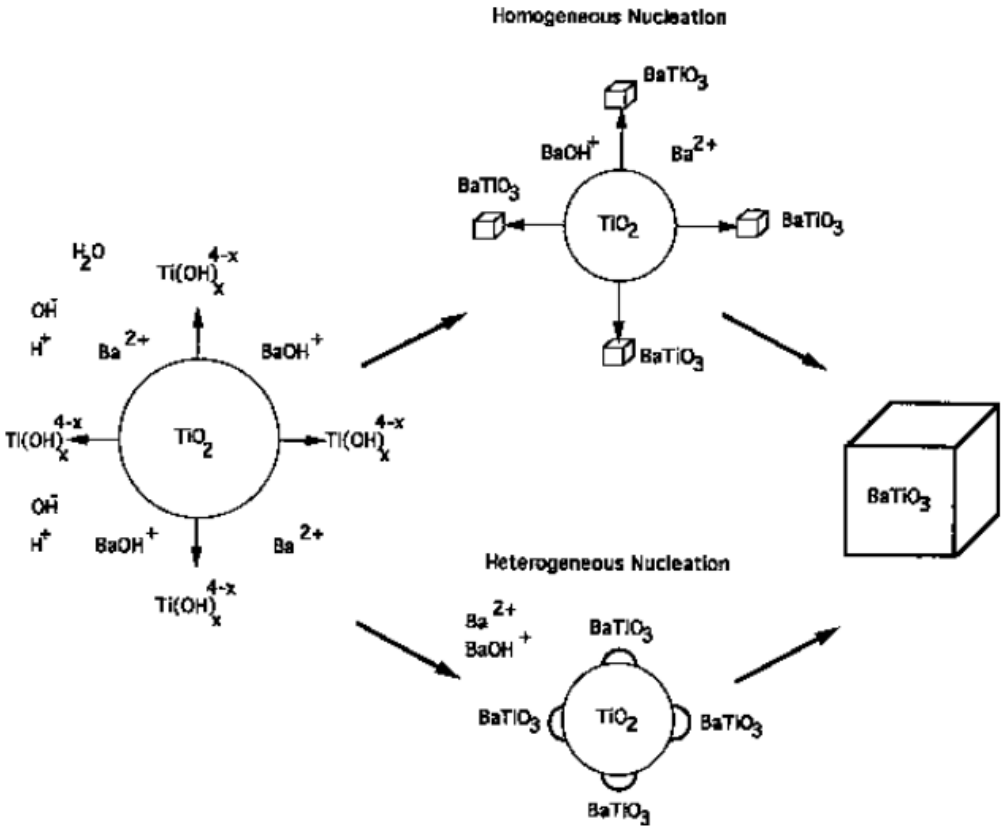

Figure 2.7: Dissolution-precipitation reaction mechanism [54,57].

Eckert et al. [54] observed that the mechanism evolved from a dissolution–precipitation process at the beginning of the reaction to an *in-situ* transformation mechanism for longer reaction times. The reason for several contradictive experimental observations in the literatures is probably the difference from the hydrothermal conditions. Now, in order to quickly synthesize the tetragonal $BaTiO_3$ powders by hydrothermal method, the strong basic solution as better choice [78, 88-91]. Feng et al. [92] Confirmation the hydrothermal reaction mechanism in the strong basic solution is important for the choice of the best precursor for the various particle sizes $BaTiO_3$ powder.

The reaction mechanism between $Ba(OH)_2$ and TiO_2 is a common process in which $BaTiO_3$ particles were obtained during other solution processes. Hertl [80]

investigated the kinetics of the barium titanate formation from $Ba(OH)_2$ and TiO_2, which assumes that the dissolved Ba^{2+} or $Ba(OH)^+$ ions react chemically with titanium precursor and $BaTiO_3$ is formed by heterogeneous nucleation on its surface. Eckert et al. [54] showed that dissolution–precipitation was the dominant mechanism throughout barium titanate synthesis and also analyzed the formation kinetics by using the Johnson–Mehl–Avrami equation. Testino et al. [39] proposed kinetic models which were based on the fundamental equations describing nucleation and growth. The investigation of the formation mechanism of barium titanate is useful in the design of the nanoparticles preparation process.

2.2.3. Reduced Graphene Oxide (rGO):

Reducing graphene oxide to produce reduced graphene oxide (hitherto referred to as rGO), is an extremely vital process as it has a large impact on the quality of the rGO produced, and therefore will determine how close rGO will come, in terms of structure, to pristine graphene. In large scale operations where scientific engineers need to utilize large quantities of graphene for industrial applications such as energy storage, rGO is the most obvious solution, due to the relative ease in creating sufficient quantities of graphene to desired quality levels.

As you would expect, there are a number of ways reduction can be achieved, though they are all methods based on chemical, thermal or electrochemical means. Some of these techniques are able to produce very high quality rGO, similar to pristine graphene, but can be complex or time consuming to carry out.
In the past, scientists have created rGO from GO by:

- Treating GO with hydrazine hydrate and maintaining the solution at 100 for 24 hours
- Exposing GO to hydrogen plasma for a few seconds
- Exposing GO to another form of strong pulse light, such as those produced by xenon flashtubes
- Heating GO in distilled water at varying degrees for different lengths of time
- Combining GO with an expansion-reduction agent such as urea and then heating the solution to cause the urea to release reducing gases, followed by cooling

- Directly heating GO to very high levels in a furnace
- Linear sweep voltammetry

> Note: These are just a sample of the numerous methods that have been attempted so far. Reducing GO by using chemical reduction is a very scalable method, but unfortunately the rGO produced has often resulted in relatively poor yields in terms of surface area and electronic conductibility. Thermally reducing GO at temperatures of 1000℃ or more creates rGO that has been shown to have a very high surface area, close to that of pristine graphene even.

Unfortunately, the heating process damages the structure of the graphene platelets as pressure between builds up and carbon dioxide is released. This also causes a substantial reduction in the mass of the GO (figures around 30% have been mentioned), creating imperfections and vacancies, and potentially also having an effect on the mechanical strength of the rGO produced.

The final example given above could eventually be the future of large scale production of rGO. Electrochemical reduction of graphene oxide is a method that has been shown to produce very high quality reduced graphene oxide, almost identical in terms of structure to pristine graphene, in fact.

This process involves coating various substrates such as Indium Tin Oxide or glass with a very thin layer of graphene oxide. Then, electrodes are placed at each end of the substrate, creating a circuit through the GO. Finally, linear sweep voltammetry is carried out on the GO in a sodium phosphate buffer at various voltages; at 0.6 volts reduction began, and maximum reduction was observed at 0.87 volts.

In recent experiments the resulting electrochemically reduced graphene oxide showed a very high carbon to oxygen ratio and also electronic conductivity readings higher than that of silver (8500 S/m, compared to roughly 6300 S/m for silver). Other primary benefits of this techniques are that there are no hazardous chemicals used, meaning no toxic waste to dispose of. Unfortunately, the scalability of this technique has come into question due to the difficulty in depositing graphene oxide onto the electrodes in bulk form. Ultimately, once reduced graphene oxide has been produced, there are ways that we can functionalise rGO for use in different applications. By treating rGO

with other chemicals or by creating new compounds by combining rGO with other two dimensional materials, we can enhance the properties of the compound to suit commercial applications

2.2.4. Thermodynamic modeling of hydrothermal synthesis of $BaTiO_3$

Lencka and Riman [57] presented thermodynamic model of electrolyte solutions in 1993, thereby giving the stability diagrams for the hydrothermal synthesis of $BaTiO_3$ to predict the optimum synthesis conditions viz., feedstock composition, pH, temperature and pressure to minimize the need for trail-and-error experimentation. The diagrams show the regions of reagent concentrations and pH for which various species predominate in the system indicating thermodynamically stable products. The stability diagrams also show predominance fields for several species as a function of pH and total molality of reactant species in the solution at constant temperature. All possible reactions that may occur in the hydrothermal medium are summarized in Table 2.I.

Rimen et al. [93] calculated the stability diagram for the hydrothermal system at 160 °C obtained by mixing barium hydroxide and titanium dioxide with a stoichiometric molar Ba/Ti ratio equal to one (Figure 2.8). The total input concentration of the Ba precursor and the solution pH adjusted by KOH are used as independent variables. It should be noted that all concentrations are expressed in molality (i.e. number of moles per 1 kg of H_2O) because it can be measured more accurately and precisely than molarity.

The solid curve in Figure 2.8 corresponds to the incipient precipitation (solubility curve) boundary for $BaTiO_3$. In the calculations, an equilibrium point is assumed to lie on the incipient precipitation boundary when less than 0.25% of the precursor is reacted to form a solid phase. Only one point on the solubility curve of $BaTiO_3$ corresponds to the solubility of barium titanate in water and this solubility is equal to about $8.6X10^{-4}$ M at 160 °C and pH 8.7. The pH values correspond to the temperature of the experiment. The formation of $BaTiO_3$ is dependent on pH. Crystalline $BaTiO_3$ can be obtained at pH higher than ca. 8.0 for the input concentration of TiO_2 equal to 1M. The stability of $BaTiO_3$ also increases with rising pH, which means, the solubility of barium titanate decreases with increasing pH.

Table 2.1: Reaction equilibria in the Ba-Ti hydrothermal systems with TiO_2 and $Ba(OH)_2$ as starting materials [57].

$H_2O \leftrightarrows H^+ + OH^-$	(1)
$TiO_{2(s)} \leftrightarrows OH^- + HTiO_3^-$	(2)
$Ba(OH)_{2(s)} \leftrightarrows Ba^{2+} + 2OH^-$	(3)
$BaOH^+ \leftrightarrows Ba^{2+} + OH^-$	(4)
$BaTiO_{3(s)} + H_2O \leftrightarrows Ba^{2+} + 2OH^- + TiO_{2(s)}$	(5)
$Ba(OH)_2 \cdot 8H_2O_{(s)} \leftrightarrows Ba^{2+} + 2OH^- + 8H_2O$	(6)
$BaO_{(s)} + 2H^+ \leftrightarrows Ba^{2+} + H_2O$	(7)
$Ba_2TiO_{4(s)} + 2H_2O = 2Ba^{2+} + 4OH^- + TiO_{2(s)}$	(8)
$CO_{2(g)} \leftrightarrows CO_{2(aq)}$	(9)
$CO_2(aq) + H_2O \leftrightarrows H^+ + HCO_3^-$	(10)
$HCO_3^- \leftrightarrows H^+ + CO_3^{2-}$	(11)
$BaCO_{3(s)} \leftrightarrows Ba^{2+} + CO_3^{2-}$	(12)
$BaCO_{3(aq)} \leftrightarrows Ba^{2+} + CO_3^{2-}$	(13)
$BaHCO_3^+ \leftrightarrows Ba^{2+} + HCO_3^-$	(14)
$Ti^{4+} + H_2O \leftrightarrows TiOH^{3+} + H^+$	(15)
$TiOH^{3+} + H_2O \leftrightarrows Ti(OH)_2^{2+} + H^+$	(16)
$Ti(OH)_2^{2+} + H_2O \leftrightarrows Ti(OH)^{3+} + H^+$	(17)
$Ti(OH)^{3+} + H_2O \leftrightarrows Ti(OH)_{4(aq)} + H^+$	(18)
$Ti(OH)_{4(aq)} \leftrightarrows TiO_{2(s)} + 2H_2O$	(19)

At the solubility curve, the yield of barium titanate is very small and it increases as we move beyond the solubility curve into the solid-liquid region, which reaches at least 99% in the shaded area of Figure 2.8. The yield is calculated by dividing the number of moles of the product by the total number of moles of the input metal

precursor. The shaded area in Figure 2.8 shows the range of input precursor concentrations and equilibrium pH that can produce 99% phase-pure $BaTiO_3$ at 160 °C.

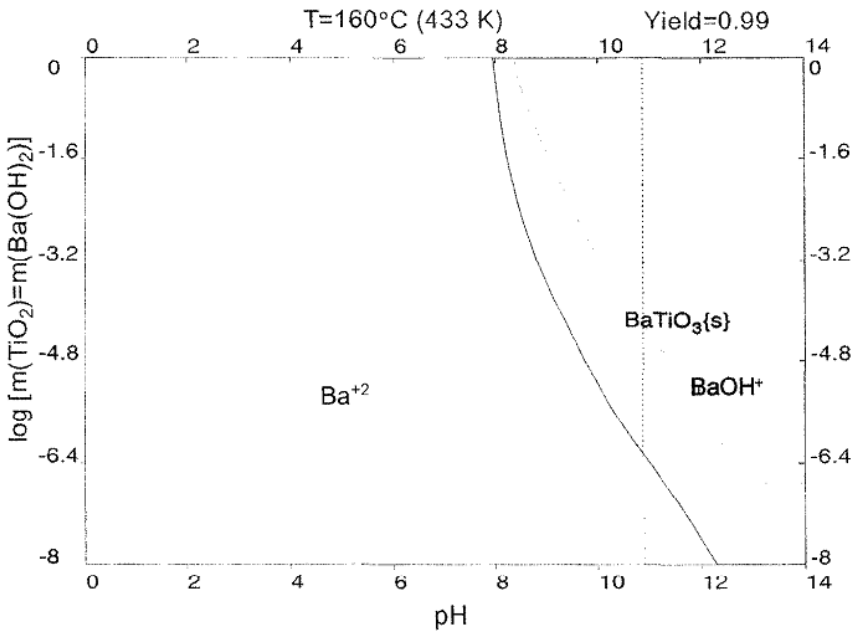

Figure 2.8: Calculated yield diagram for Ba-Ti system at 160 °C as a function of the equilibrium solution pH, $Ba(OH)_2$ and TiO_2 (rutile) are used as precursors and the ratio of Ba/Ti is equal to 1. The solid line denotes the incipient precipitation boundary for $BaTiO_3$; in the area above the solid line, $BaTiO_3$ and TiO_2 coexist. The shaded area corresponds to the BaTi yield >99%. The dotted line separates regions dominated by different aqueous species, which in this case are Ba^{2+} and $BaOH^+$ [93].

The dotted line on the yield diagram corresponds to the loci where two aqueous species have equal concentrations, which in this case corresponds to Ba^{2+} and $BaOH^+$. At 160 °C, Ba^{2+} dominates at pH below 10.8 and it becomes hydrolyzed to $BaOH^+$ above this pH. There is also titanium complexes present in this system (Table 2.I)**.** However, their concentrations within the stability region corresponding to 99% yield of $BaTiO_3$ are very small (~10^{-9}-10^{-8}M) and do not change significantly with mineralizer concentration or increases in temperature. As pH increases (increasing mineralizer concentrations), even the amount of soluble barium decreases to very low values. The stability diagrams illustrate the effect of process variables such as concentration of Ba, pH, temperature and

the Ba/Ti ratio on the synthesis of barium titanate. Aksay et al. [94] have prepared nanometer sized $BaTiO_3$ particles under hydrothermal conditions by dispersing TiO_2 powders in a concentrated aqueous solution of $Ba(OH)_2$. The TiO_2 particles dissolve in the aqueous $Ba(OH)_2$ solution and lead to the nucleation of nanometer-sized cubic phase $BaTiO_3$ particles. In concentrated solutions, $BaTiO_3$ particles grow through multiple clustering. SEM micrographs illustrates the morphology of $BaTiO_3$ particles synthesized by hydrothermal process at different ratios of Ba:Ti at 55, 75 and 95 °C (Figure 2.9).

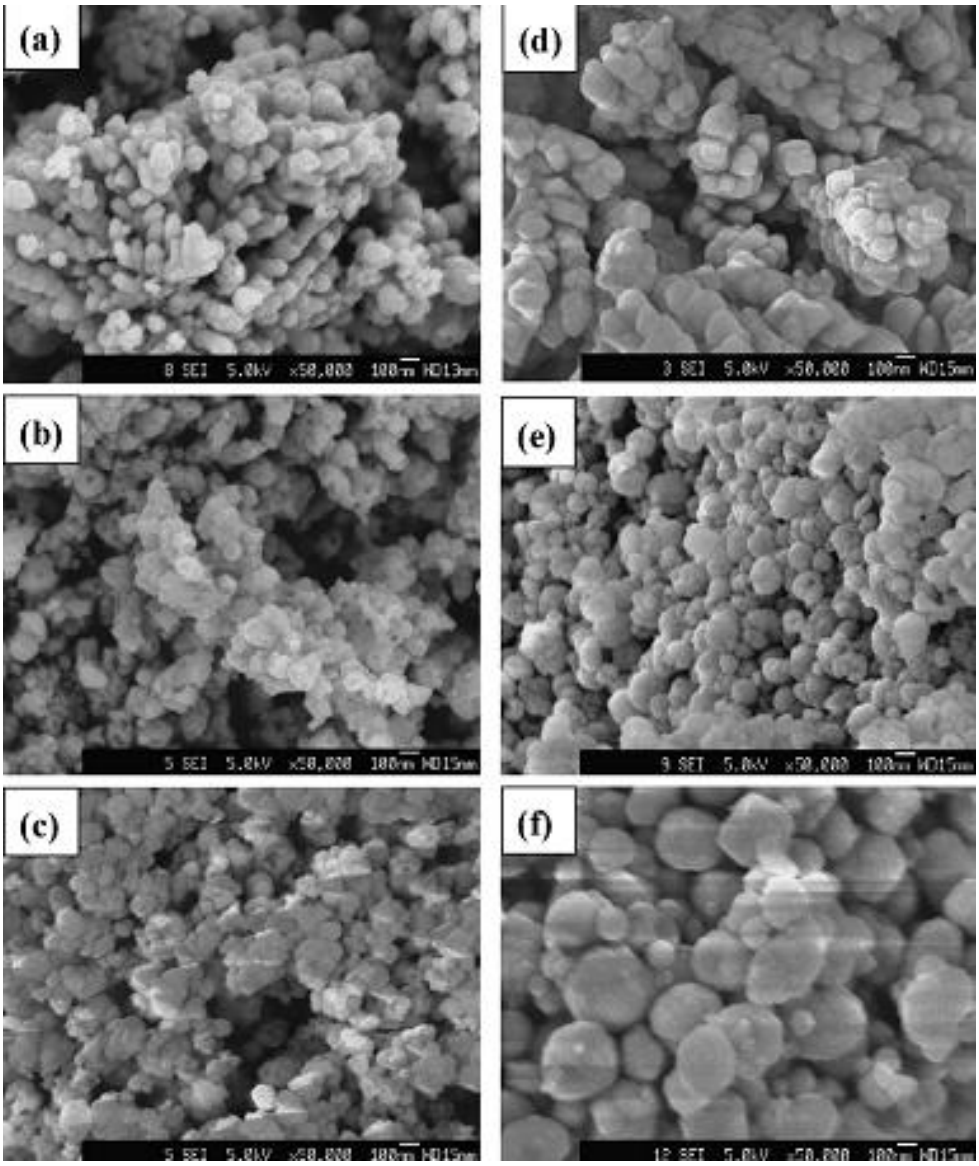

Figure 2.9.: SEM micrographs of the different reaction conditions: (a), (b), and (c) corresponded to Ba/Ti =1, Ba/Ti =2, and Ba/Ti =4 at 95 °C, (d) and (e) corresponded to Ba/Ti =2 and Ba/Ti =4 at 75 °C, (f) corresponded to Ba/Ti =4 at 55 °C, respectively [95].

The effects of synthesis temperature, pH of the reaction medium, and the Ba/Ti ratio on the particle size and morphology have also been investigated extensively [96-99]. In concentrated solutions, the consumption of OH- ions is caused by the following predominant reactions:

$$M^{2+} + TiO_2 + 2OH^- \leftrightarrows MTiO_3 + H_2O$$

Thus, 2M OH^- is consumed for the synthesis of 1M $MTiO_3$, and only a relatively small amount of OH^- is necessary to ensure correct pH for respective alkaline earth. Unlike the synthesis with nitrates, the use of metal hydroxide precursors at high concentrations does not require the addition of a mineralizer because the necessary concentration of OH^- groups is readily provided by the hydroxide precursor. To the contrary, at dilute concentrations identical amounts of mineralizers are needed, irrespective of whether a nitrate or a hydroxide is used as precursor. However, the required mineralizer concentration differs substantially for the three metals. This may be caused by the strong, specific effects of the chemical identity of cations on activity coefficients due to their high concentration to form alkaline-earth titanates.

2.2.5. Major application of $BaTiO_3$

1. Barium titanate is a dielectric ceramic used for capacitors
2. It is a piezoelectric material for microphones and other transducers
3. The spontaneous polarization of barium titanate is about 0.15 C/m^2 at room temperature and its Curie point is 120 °C
4. As a piezoelectric material, it was largely replaced by lead zirconate titanate, also known as PZT
5. Polycrystalline barium titanate displays positive temperature coefficient, making it a useful material for thermistors and self-regulating electric heating systems
6. Barium titanate crystals find use in nonlinear optics
7. It has high beam-coupling gain, and can be operated at visible and near-infrared wavelengths. It has the highest reflectivity of the materials used for self-pumped phase conjugation (SPPC) applications
8. It can be used for continuous-wave mixing with mill-watt-range optical power. For photorefractive applications, barium titanate can be doped by various other elements, e.g. iron

9. Thin films of barium titanate display electro-optic modulation to frequencies over 40 GHz
10. The pyroelectric and ferroelectric properties of barium titanate are used in some types of uncooled sensors for thermal cameras
11. High purity barium titanate powder is reported to be a key component of new barium titanate capacitor energy storage systems for use in electric vehicles

CHAPTER 3

MATERIALS AND METHODS

3.1. Materials

All chemicals were reagent-grade and used without further purification. Titanium dioxide powder (TiO_2; >99.90%, Merck) and barium hydroxide octahydrate ($Ba(OH)_2{\cdot}8H_2O$; 98%; Sigma-Aldrich) were used for the synthesis of $BaTiO_3$ nano powder. Formic acid (HCOOH; 85%; Merck) was used to wash the synthesized $BaTiO_3$ powder. Reduced graphene oxide (rGO) powder synthesized by reducing graphene oxide (GO) was used.

3.2. Methods

The synthesis of barium titanate was carried out in an autoclave. A weight of 19.0 g of $Ba(OH)_2{\cdot}8H_2O$ and 3.40 g TiO_2 powder were mixed in a 250-mL Teflon reaction vessel containing 60 mL of deionized water. The laboratory high-pressure reactor system/ stirred autoclave (Model limbo li, Büchi AG, Switzerland) was operated at either 100, 150, 160 or 180°C for periods ranging from 3, 5 and 7 hr. with the stirring speed set at 60 rpm. After hydrothermal reaction, the contents of the Teflon vessel was cooled to room temperature, after which the soluble impurities/adsorbed ions were removed with dilute (0.25 M) formic acid (HCOOH) solution (9.50 mL of 85% formic acid in 250 ml deionized water). The content of the Teflon reaction vessel was transferred into centrifuge bottles to separate the $BaTiO_3$ precipitate. After centrifugation at 4,000 rpm for 10 min, the supernatant was poured out and the white precipitate was washed initially with dilute formic acid solution and then with deionized water for five times. Each time the supernatant was decanted. Finally, the washed precipitate/ residue were dried in oven at 100 °C for 2 hr.

Similarly, an experiment was conducted to synthesize $BaTiO_3$ powders by using reduced graphene powder (0.025 g) at 160 °C for 7 hr in stirred autoclave. In this experiment, a weight of 21.0 g $Ba(OH)_2{\cdot}8H_2O$ and 5.0 g TiO_2 powder were mixed in a 250-mL Teflon reaction vessel containing 30 mL of deionized water.

The experimental set up is shown in Figure 3.1 and a scheme for the hydrothermal synthesis of $BaTiO_3$ in present experimentation is illustrated in Figure 3.4.

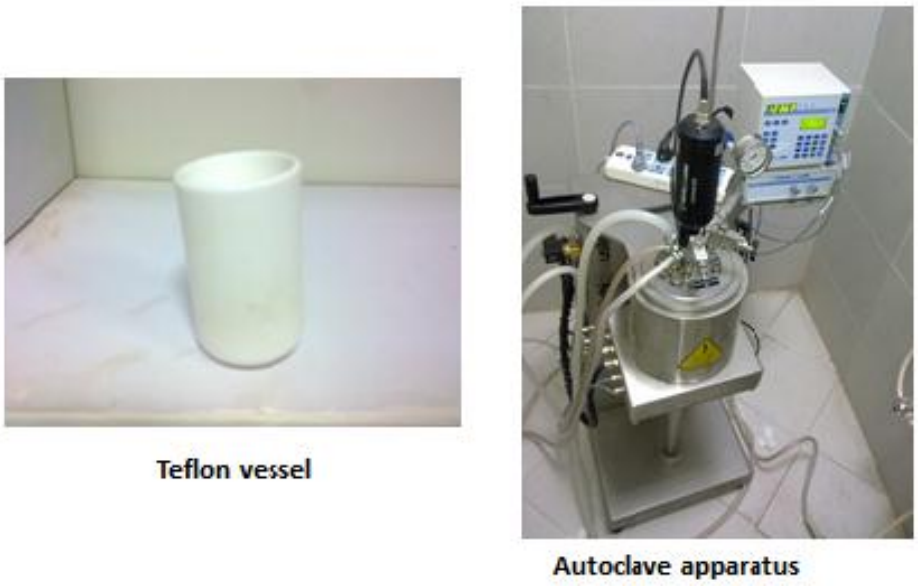

Figure 3.1: High-pressure reactor system/ stirred autoclave (Model limbo li, Büchi AG, Switzerland) and Teflon vessel used for experimental work at SCME.

3.3. Characterization of $BaTiO_3$:

3.3.1. X-ray Diffraction (XRD) Analysis:

The structural properties of the $BaTiO_3$ powder samples were characterized on a X-ray diffractometer using CuKα radiation (λ=1.54056 Å) and graphite monochromator operated at 40 kV and 30 mA. The scanning speed was 0.02° Θ at step scan of 0.25 s over the 2Θ range of 10-70°. X-ray diffractogram matching was performed in the automatic mode against JCPDS powder diffraction library, then manually to confirm the automated identification of phases.

3.3.2. Scanning Electron Microscopy (SEM):

The microstructure and particle morphology of $BaTiO_3$ powders were investigated by using scanning electron microscope (Model JEOL JSM-6490A, Japan)

with a field gun. The powder samples were placed/ mounted on Cu stub specially made for SEM analysis. The samples were sputter-coated with Au for 90 s using JFC-1500 Ion Sputtering Device. An accelerating voltage of 20 kV was used. The images were recorded at magnifications from 2,500-75,000.

Energy Dispersive X-ray Spectrometer (JED-2300 series), installed on the SEM, performed nondestructive elemental analysis of micro-areas observed by the SEM Analysis Station.

Figure 3.2: JEOL Analytical Scanning Electron Microscope (JEOL JSM-6490A)

3.3.3. Raman Spectroscopy:

The Raman spectra of synthesized $BaTiO_3$ powders were recorded using a Dongwoo Optron Micro Raman Spectrophotometer (Korea) with laser (532 nm) power of 150 mW. The system was equipped with CCD detector and monochroator M320. This part of work was performed at National Institute of Laser and Optronics (NILOP), Nilore-Islamabad.

3.3.4. Fourier transforms infra-red spectroscopy:

FT-IR spectra of $BaTiO_3$ powders were recorded using a Nicolet 6700 FT-IR Spectrometer (Thermo Electron Corporation, UK) with CsI detector and ATR-smart accessory. This part of work was performed at PIEAS, Nilore-Islamabad.

3.3.5. Impedance Spectroscopy

The impedance spectroscopy of pressed pellets of $BaTiO_3$ powders was performed using a computer interfaced impedance analyzer (Agilent E4980A LCR meter). The pellets of $BaTiO_3$ powders were prepared by mechanical pressing (STENHØJ 25, Denmark) at 20 tones force. The width and diameter of pellet was 2 mm and 10 mm, respectively. The contacts of $BaTiO_3$ pellets were made with silver paste as shown in Figure 3.4 and the measurements were made with impedance analyzer. In these measurements, frequency of applied ac signal was varied from 1 KHz to 2 MHz and amplitude of the signal was 1 V. The impedance results were analyzed using Z-View software. This part of work was carried out at PIEAS, Islamabad.

Figure 3.3: $BaTiO_3$ powder pellet prepared for impedance analysis.

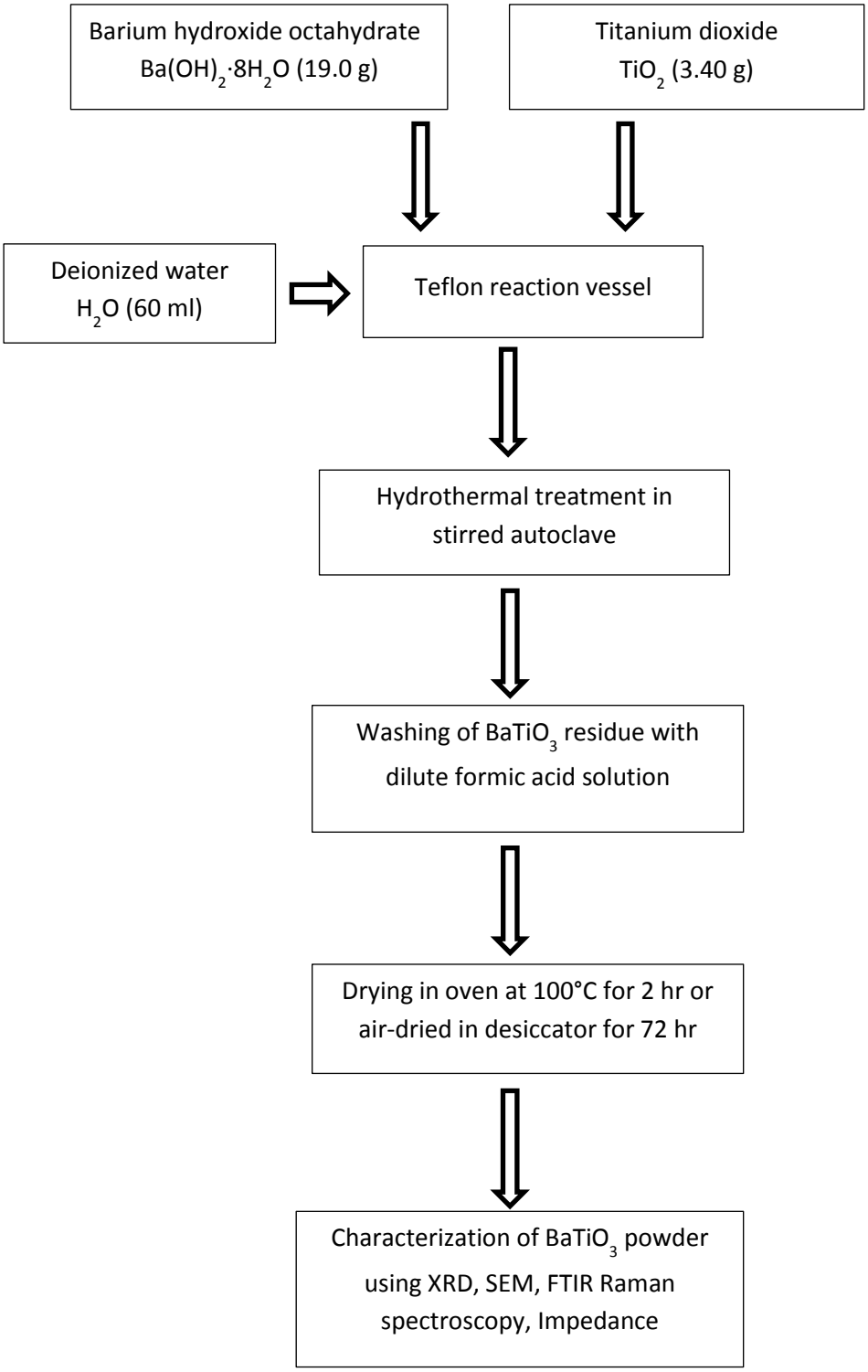

Figure 3.4: Flow sheet of the hydrothermal synthesis of $BaTiO_3$ nano powder using stirred autoclave

CHAPTER 4
RESULTS AND DISCUSSION

4.1. Hydrothermal synthesis of $BaTiO_3$ powder:

Barium titanate ($BaTiO_3$) fine particles were prepared by hydrothermal synthesis using stirred autoclave. The synthesis was performed in the temperature range between 100 and 180 °C for 3 to 7 hr. $BaTiO_3$ powder produced according to the following chemical reactions involved in hydrothermal process:

$$Ba(OH)_2 \leftrightarrows Ba^{2+} + 2OH^- \quad (1)$$

$$CO_2 + 2OH^- \leftrightarrows CO_3^{2-} + H_2O \quad (2)$$

$$TiO_2 \cdot nH_2O + 2OH^- \leftrightarrows Ti(OH)_6^{2-} + (n-2)H_2O \quad (3)$$

$$Ba^{2+} + Ti(OH)_6^{2-} \leftrightarrows BaTiO_3 + 3H_2O \quad (4)$$

$$Ba^{2+} + CO_3^{2-} \leftrightarrows BaCO_3 \quad (5)$$

According to the above chemical reaction equilibrium, increase in OH^- concentration and reaction temperature can facilitate the formation of $BaTiO_3$ (reactions 3 and 4), and the formation of $BaCO_3$ (reactions 2 and 5). The formation of $BaCO_3$ will decrease the concentration of Ba^{2+} ions in the reaction solution resulting influence on the formation of $BaTiO_3$. Increasing Ba/Ti ratio in precursor, the equilibrium formula (reaction 4) will move towards the formation of $BaTiO_3$; consequently, the Ba/Ti ratio of the $BaTiO_3$ particle will increase. The overall net chemical reaction for the synthesis of $BaTiO_3$ can be described as below:

$$Ba(OH)_2 + TiO_2 \rightarrow BaTiO_3(\text{crystallite}) + H_2O \quad (6)$$

The yield of the reaction (6) is controlled by the solubility of $Ba(OH)_2$; if the limit of solubility of $Ba(OH)_2$ is reached before completion, the reaction stops, and the yield stabilizes. Assuming that the pH is ensured only by the unreacted $Ba(OH)_2$, this situation also corresponds to the stabilization of the pH at a critical value.

The physical appearance of the synthesized $BaTiO_3$ fine powders was yellowish white (Figure 4.1). The hydrothermal synthesis technique involves a simple reaction of barium hydroxide ($Ba(OH)_2$) with crystalline or hydrous titania (TiO_2) in an aqueous solution in a stirred autoclave. During this synthesis process, the reaction mechanism

between $Ba(OH)_2$ and TiO_2 is a common process in which $BaTiO_3$ powders were obtained. Hertl investigated the kinetics of the barium titanate formation from $Ba(OH)_2$ and TiO_2, which assumed that the dissolved Ba^{2+} or $Ba(OH)^+$ ions react topo chemically with the titanium precursor and the $BaTiO_3$ is formed by heterogeneous nucleation on its surface [18].

Figure 4.1: Photograph of synthesized $BaTiO_3$ powder

4.2. Characterization of $BaTiO_3$ powders:

4.2.1. X-Ray Diffraction (XRD) Analysis:

The typical XRD pattern of the synthesized $BaTiO_3$ powders at 160 °C for 7 hr is shown in Figure 4.2. It is shown that the XRD patterns fit well with the peak positions of standard cubic phase $BaTiO_3$. The appearance of X-ray diffraction peaks at °2Θ = 22.00 (100), 31.35 (110), 38.65 (111), 44.95 (200), and 55.80° (211) can be indexed to the cubic structure $BaTiO_3$ with lattice constant to be a = 4.04 Å, which is in good agreement with the standard reported data (JCPDS Card No. 31-0174). It is clear that the X-ray diffraction peak (110) is sharper and stronger. This XRD patterns indicate that $BaTiO_3$ was successfully synthesized by hydrothermal process. Since XRD patterns showed appreciable peak broadening presumable due to small particle size, which was

evidence to the cubic structure. The presence of unreacted TiO_2 was identified as an impurity in the synthesized $BaTiO_3$ powder (Figure 4.2).

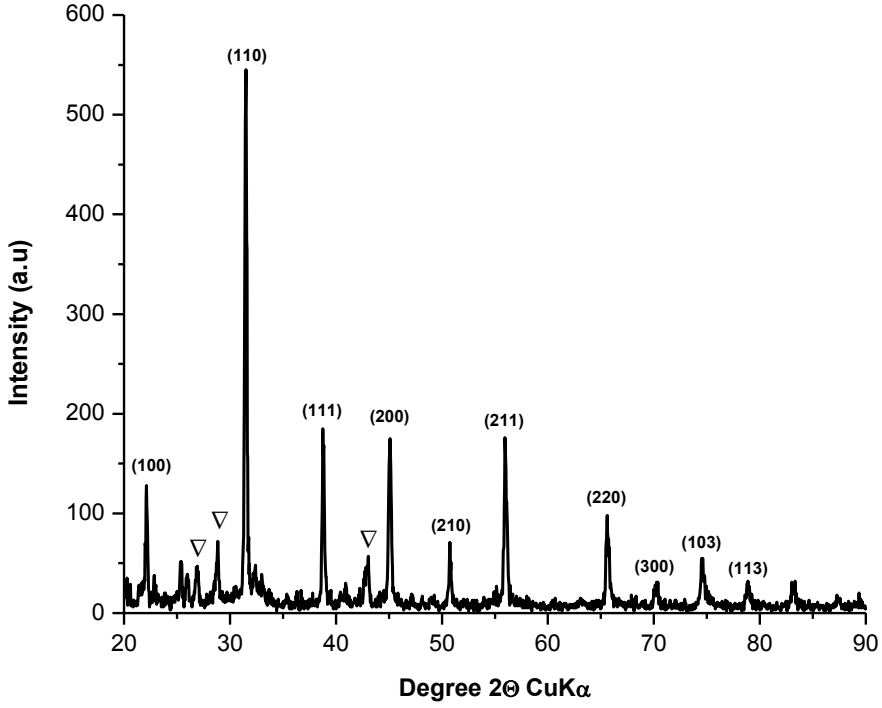

Figure 4.2: XRD patterns of $BaTiO_3$ powder synthesized at 160 °C for 7 hr by the hydrothermal process.

It is shown that the XRD pattern fit well with the peak positions of standard cubic- phase $BaTiO_3$. Typically, the presence of cubic form of $BaTiO_3$ is inferred from the powder diffraction patterns which exhibit single reflection (200) around a 2Θ of 45° as shown in Fig. 4.3. The presence of a tetragonal form of barium titanate is observed from the powder diffraction pattern containing two reflection (200) + (020) around a 2Θ of 45°, whereas in the cubic form only single reflection (200) is presented in this region. Therefore, the XRD pattern shown in Fig. 4.2 confirms that the synthesized $BaTiO_3$ is composed of cubic form of barium titanate powder.

The diffraction peaks are sharp and strong in the XRD pattern, which indicate the crystallinity of the product. The crystallinity of $BaTiO_3$ (cubic) was estimated by

measuring the XRD peak intensity (100) at 2Θ=22.16°. The unit cell parameter for the crystalline $BaTiO_3$ is determined to be a=3.994Å and c=4.035Å which are consistent with the literature data of JCPDS (31-1741). The XRD pattern showed the presence of TiO_2 (∇) as an impurity in the synthesized $BaTiO_3$ powder as shown in Figure 4.2.

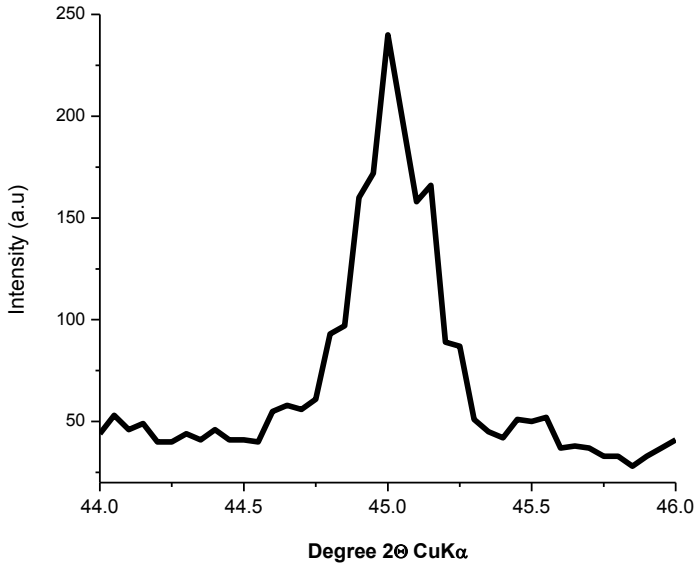

Figure 4.3: XRD patterns of $BaTiO_3$ powders synthesized at 160 °C for 7 hr showing clearly reflections (200) of the cubic form.

A shape factor is used in X-ray diffraction and crystallography to correlate the size of sub-micrometer particles, or crystallites, in a solid to the broadening of a peak in a diffraction pattern. In the Scherer's equation:

$$\tau = \frac{K\lambda}{\beta \cos\theta}$$

where '*K*' is the shape factor usually taken as 0.89; 'λ' is the X-ray wavelength of CuKα radiation (λ = 0.15406 nm); 'β' is the line broadening at half the maximum intensity (FWHM) in radians, and 'θ' is the Bragg's angle; 'τ' is the mean size of the ordered (crystalline) domains, which may be smaller or equal to the grain size. The dimensionless shape factor '*K*' has a typical value of about 0.9, but varies with the actual shape of the crystallite. The Scherer equation is limited to nano-scale particles. It is not

applicable to grains larger than about 0.1 μm, which precludes those observed in most metallographic and ceramographic microstructures.

The average particle size of $BaTiO_3$ powder synthesized was calculated to be ~31 nm from the broadening of the corresponding XRD peaks using the Scherrer equation, which conformed reasonably well to the literature value [100]. Typically, the presence of cubic form of $BaTiO_3$ is inferred from the powder diffraction patterns which exhibit single reflection (200) around a 2Θ of 45° as shown in Fig. 4.3.

A. Synthesis of $BaTiO_3$ at 100°C:

The XRD patterns of $BaTiO_3$ powders synthesized at 100 °C for 5 hr and 7 hr through hydrothermal process exhibiting that both the products are of good crystallinity (Figure 4.4). The diffraction peaks are sharp and strong in the XRD pattern, which indicate the crystallinity of the product. Since, XRD patterns showed appreciable peak broadening presumable due to small particle size, which was evidence to the cubic structure. The presence of $BaCO_3$, Ba_2TiO_4 and un-reacted TiO_2 phases were also identified as impurities in the $BaTiO_3$ powders. The peak intensity of $BaCO_3$ was decreased with an increase in reaction time during hydrothermal process. $BaCO_3$ can be removed by a washing process during synthesis process.

The average particle size of $BaTiO_3$ powder synthesized at 100 °C for 5 hr reaction time was calculated to be ~31 nm from the broadening of the corresponding XRD peaks using the Scherrer equation, which conformed reasonably well to the literature value [100]. These XRD patterns indicate that $BaTiO_3$ was successfully synthesized by hydrothermal process. Since XRD patterns showed appreciable peak broadening presumable due to small particle size, which was evidence to the cubic structure.

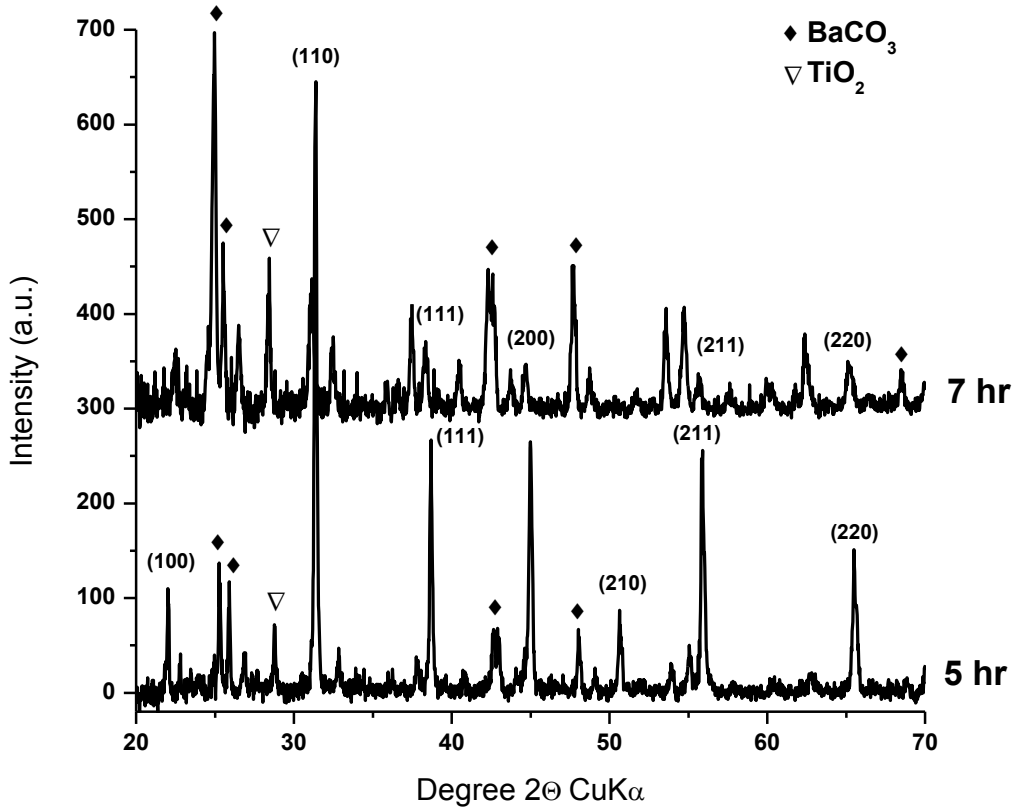

Figure 4.4: XRD patterns of $BaTiO_3$ powders synthesized by the hydrothermal process at 100 °C for 5 and 7 hr. The presence of $BaCO_3$ (♦) and Ba_2TiO_4 (∇) and un-reacted TiO_2 were also identified in the $BaTiO_3$ powders.

B. Synthesis of $BaTiO_3$ at 150°C:

The XRD patterns of $BaTiO_3$ powders synthesized at 150 °C for 5 hr and 7 hr exhibited that both the products are of good crystallinity (Figure 4.5). Since, XRD patterns showed appreciable peak broadening presumable due to small particle size, which was evidence to the cubic structure. The presence of $BaCO_3$ was also identified as an impurity in the $BaTiO_3$ powders which can be removed by a washing process during synthesis process.

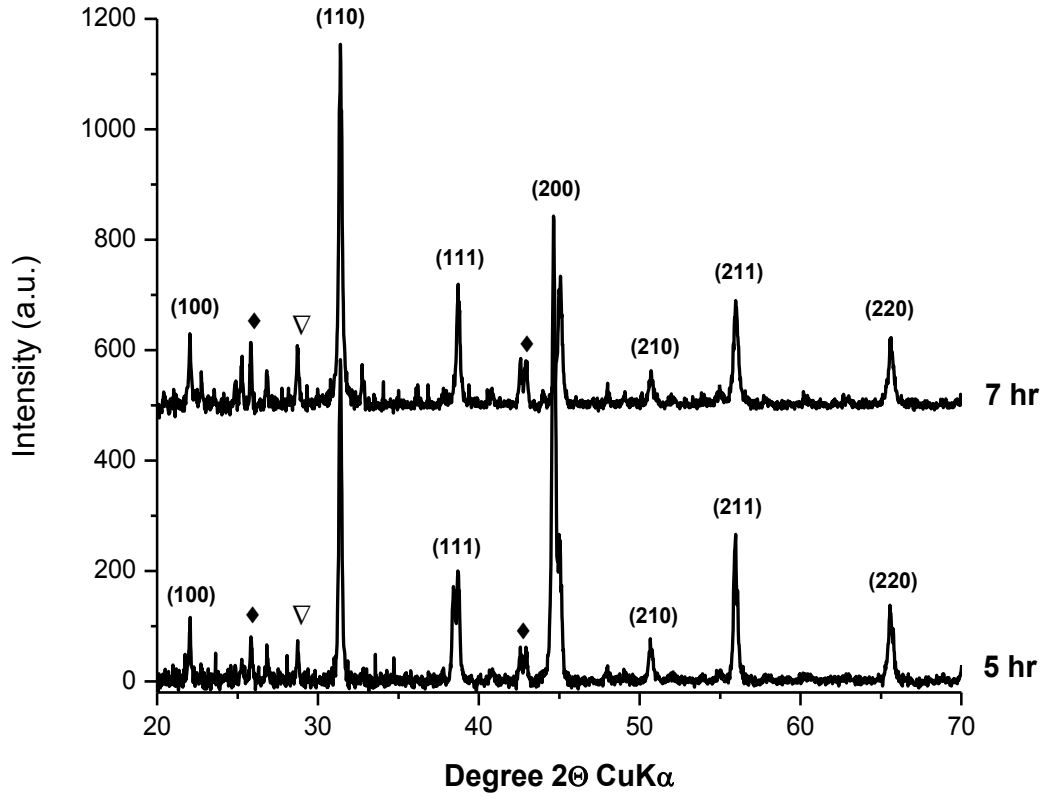

Figure 4.5: XRD patterns of $BaTiO_3$ powders synthesized by the hydrothermal process at 150 °C for 5 and 7 hr. The presence of $BaCO_3$ (♦) was identified in the $BaTiO_3$ powders.

C. Synthesis of $BaTiO_3$ at 180°C:

The XRD patterns of $BaTiO_3$ powders synthesized at 180 °C for 3 hr and 7 hr through hydrothermal process exhibiting that both the products are of good crystallinity (Figure 4.6). The diffraction peaks are sharp and strong in the XRD pattern, which indicate the crystallinity of the product. Since, XRD patterns showed appreciable peak broadening presumable due to small particle size, which was evidence to the cubic structure. The presence of $BaCO_3$ phase was only identified in the product obtained at 7 hr reaction time at 180°C. The presence of un-reacted TiO_2 phase was also identified in both the XRD patterns.

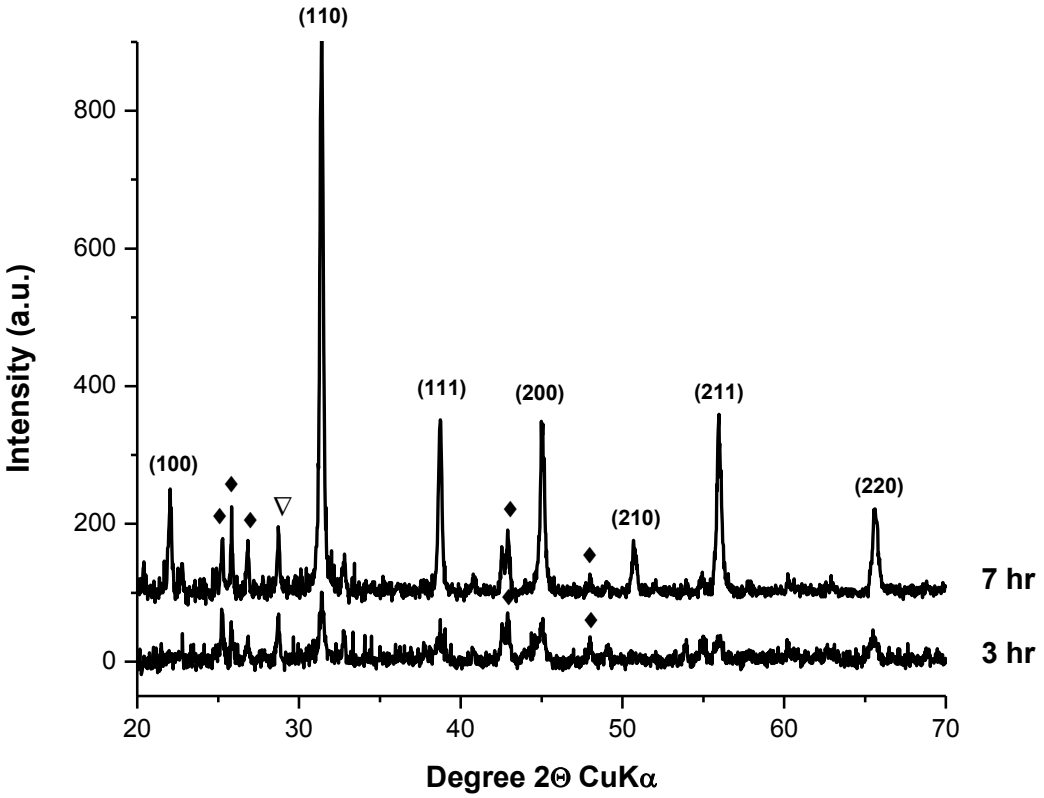

Figure 4.6: XRD patterns of $BaTiO_3$ powders synthesized by the hydrothermal process at 180 °C for 3 and 7 hr. The presence of $BaCO_3$ (♦) was identified in the $BaTiO_3$ powders.

The XRD patterns of $BaTiO_3$ powders synthesized at 100, 150 and 180 °C for 7 hr reaction time exhibited that X-ray diffraction peak intensities at °2Θ = 22.00 (100), 31.35 (110), 38.65 (111), 44.95 (200), and 55.80° (211) of the products increased with increase in reaction temperature during hydrothermal process (Figure 4.7). The presence of $BaCO_3$ phase was identified in the products as impurity. This XRD patterns indicate that $BaTiO_3$ was successfully synthesized by hydrothermal process. Since XRD patterns showed appreciable peak broadening presumable due to small particle size, which was evidence to the cubic structure. The XRD patterns of $BaTiO_3$ powders synthesized at 100, 150 and 180 °C for 7 hr clearly showed shifting of reflections around 45° 2Θ (200) (Figure 4.8).

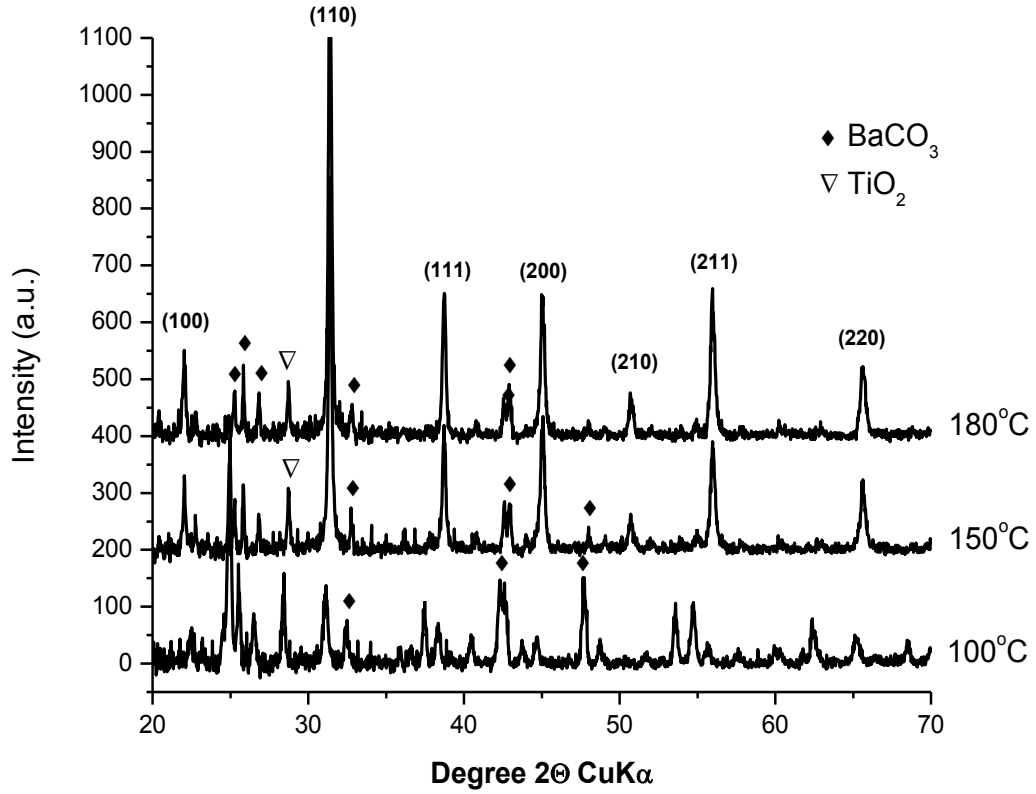

Figure 4.7: XRD patterns of $BaTiO_3$ powders synthesized by the hydrothermal process at reaction temperature of 100, 150 and 180 °C for 7 h reaction time.

When the reaction temperature of $BaTiO_3$ synthesis was increased from 100 °C to 150 and 180 °C during hydrothermal process, the peaks in the XRD patterns are strong and sharp, which indicate relatively high crystallinity of the powders (Figures 4.2, 4.4-4.7). It is shown that all patterns fit well with the peak positions of standard cubic phase $BaTiO_3$. The formation of $BaCO_3$ as impurity was not detected as the reaction temperature and time increased during the hydrothermal synthesis process. Barium carbonate ($BaCO_3$) might be decomposed to barium oxide (BaO) and carbon dioxide (CO_2) at higher reaction temperatures during hydrothermal process and its reaction with TiO_2 could produce $BaTiO_3$ according to following chemical reactions:

$$BaCO_3 \rightarrow BaO + CO_2$$

$$BaO + TiO_2 \rightarrow BaTiO_3$$

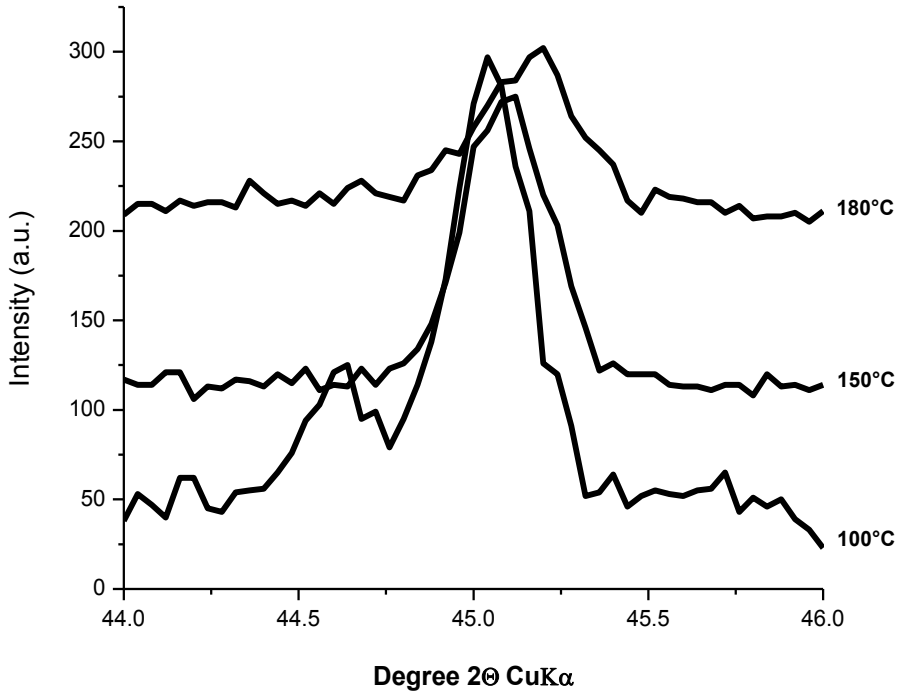

Figure 4.8: XRD patterns of $BaTiO_3$ powders synthesized by the hydrothermal process at 100, 150 and 180 °C for 7 h reaction time showing clearly shifting of reflections around 45° 2Θ (200) with increase in reaction temperature.

These XRD patterns indicate that cubic phase $BaTiO_3$ powder is successfully synthesized by using TiO_2 and barium hydroxide during hydrothermal process. Figure 4.7 presents the X-ray diffraction patterns of the samples prepared at 100, 150 and 180 °C for 7 h. It is shown that the XRD patterns of all the samples fit well with the peak positions of standard cubic phase $BaTiO_3$. It is clear that the X-ray diffraction peak (110) becomes sharper and stronger with increase in the reaction temperature. The XRD data of synthesized $BaTiO_3$ powders could be confirmed using the Raman spectroscopy.

D. Synthesis of $BaTiO_3$ in the presence of Reduced Graphene Oxide (RGO):

The XRD pattern of $BaTiO_3$ powder synthesized at 160 °C for 7 hr reaction time in the presence of reduced graphene oxide (RGO) is shown in Figure 4.9. It is shown that the XRD pattern fits well with the peak positions of standard cubic phase $BaTiO_3$. The appearance of X-ray diffraction peaks at °2Θ = 22.00 (100), 31.35 (110), 38.65 (111),

44.95 (200), and 55.80° (211) can be indexed to the cubic structure $BaTiO_3$ with lattice constant to be a = 4.04 Å, which is in good agreement with the standard reported data (JCPDS Card No. 31-0174). It is clear that the X-ray diffraction peak (110) is sharper and stronger. This XRD pattern indicates that $BaTiO_3$ was successfully synthesized by hydrothermal process.

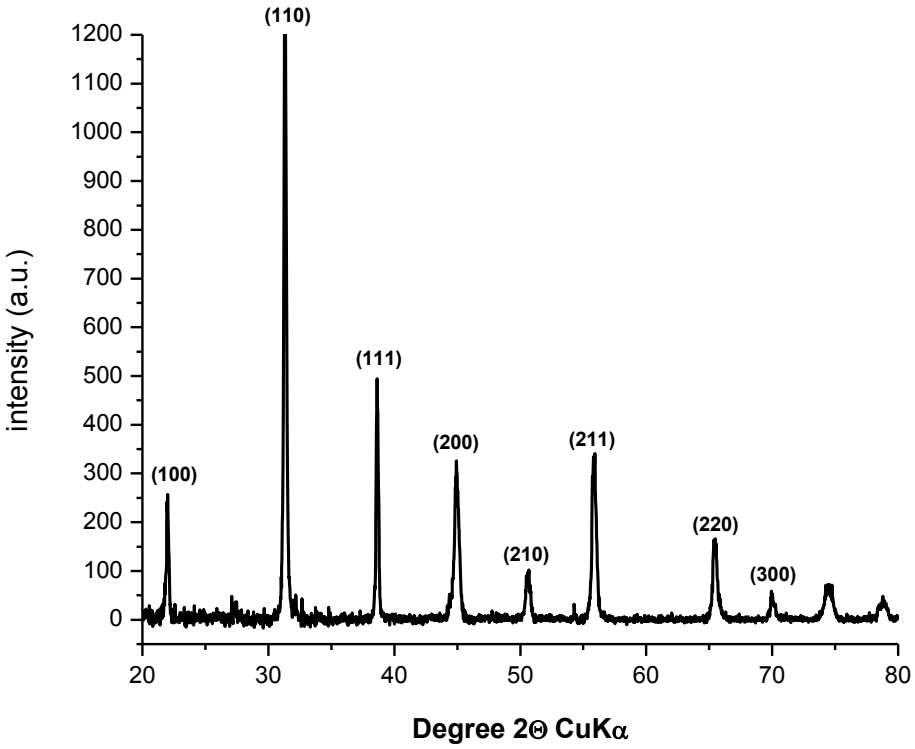

Figure 4.9: XRD pattern of $BaTiO_3$ powder synthesized at 160 °C for 7 hr reaction time in the presence of reduced graphene oxide (RGO) by the hydrothermal process.

Since, XRD pattern showed appreciable peak broadening presumable due to small particle size, which was evidence to the cubic structure. It is shown that the XRD pattern fit well with the peak positions of standard cubic- phase $BaTiO_3$. The diffraction peaks are sharp and strong in the XRD pattern, which indicates the crystallinity of the product. It is clear from the XRD pattern that the synthesis reaction is complete and the

presence of $BaCO_3$ as well as residual unreacted TiO_2 as impurity in the synthesized $BaTiO_3$ powder was not detected.

4.2.2. Raman Spectroscopy:

Raman spectroscopy is a highly sensitive spectroscopic technique to probe the local structure of atoms in materials. $BaTiO_3$ has five atoms and fifteen degrees of freedom per unit cell. $BaTiO_3$ single crystals at room temperature have a tetragonal perovskite structure (space group *P*4mm) with one formula unit per unit cell. Only below the Curie point (near 120°C), $BaTiO_3$ become ferroelectric. In the interval 120-1460 °C, $BaTiO_3$ monorystals take the paraelectric cubic perovskite structure (space group *P*m3m). The vibrational modes in the cubic phase $BaTiO_3$ are 3*F*1u + *F*2u [104]. *F*2u and *F*1u are not Raman active modes because the first-order Raman scattering is symmetrically forbidden in bulk $BaTiO_3$.

The lowered unit cell symmetry of the tetragonal phase $BaTiO_3$ causes that each of the three *F*1u modes splits into A1 + E, and the *F*2u mode splits into B1 + E. The vibrational modes in this structure are 3A +4E+B1. Therefore, the tetragonal phase $BaTiO_3$ can be distinguished displaying Raman active modes by vibrational spectroscopy [105]. Based on crystallography, only infrared active bands without first-order Raman activity are predicted for cubic $BaTiO_3$ whereas eight Raman-active modes, seven of which being also IR active, are expected for tetragonal $BaTiO_3$ [101-102].

The Raman scattering spectrum of the $BaTiO_3$ powder prepared at 160 °C for 7 hr is shown in Figure 4.11. The frequency covered range is from 100-1000 cm^{-1}. Raman spectrum clearly showed sharp bands at 160, 393, 510 and 633 cm^{-1}, three weak bands around 300, 945 and 981 cm^{-1} and a sharp small band at 197 cm^{-1}. Raman active modes attributed to tetragonal phase $BaTiO_3$ (714 cm^{-1} and 308 cm^{-1}) do not appear in the spectrum of synthesized $BaTiO_3$ powder.

According to Busca et al., [101], cubic phase $BaTiO_3$ exhibits a band at 516 cm^{-1}, whereas band at 523 cm^{-1} corresponds to tetragonal phase with nearly the same intensities, the stretching being a little larger for cubic. According to Lu et al., [102], $BaTiO_3$ exhibits two large bands at 520 and 716 cm^{-1} for tetragonal with nearly the same intensities. Raman active modes attributed to tetragonal $BaTiO_3$ do not appear in the

spectrum which confirms the cubic phase of the $BaTiO_3$ powder prepared at temperature 160 °C (Figure 4.11).

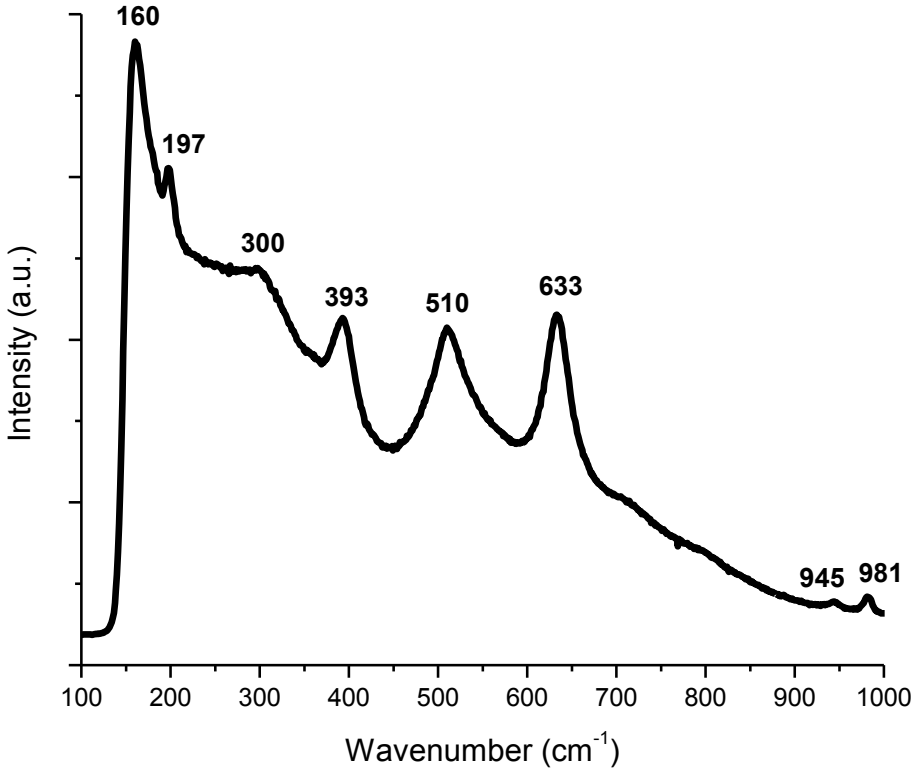

Figure 4.10: Raman spectra of $BaTiO_3$ powder prepared at 160 °C for 7 hr by hydrothermal process.

The Raman spectra of $BaTiO_3$ powders with reduced Graphene Oxide synthesized at temperature 160 °C for 7 hr reaction time are shown in Figure 4.12. The sample synthesized shows two strong Raman active modes around 270, 419 cm^{-1}, and three small sharp modes at 182, 220 and 600 cm^{-1}.

The Raman spectra of $BaTiO_3$ powders synthesized at temperature 100 °C for 5 and 7 hr reaction time are presented in Figure 4.12. The sample synthesized at 100°C for 5 hr reaction time presents small shoulder bands at around 166, 196 (a small shoulder at ~301 cm^{-1}), 394, 516, and 636 cm^{-1}. However, the band intensities of $BaTiO_3$ sample

were increased and sharp with increasing the reaction time from 5 hr to 7 hr at 100 °C. Two broad shoulder bands at 792 and 984 cm^{-1} were also appeared in the sample obtained at 7 hr reaction time. It is clear from the Raman spectra of both the samples contained bands of predominantly cubic phase $BaTiO_3$ identified by the bands around 166, 196, 394, 512, and 636 cm^{-1}.

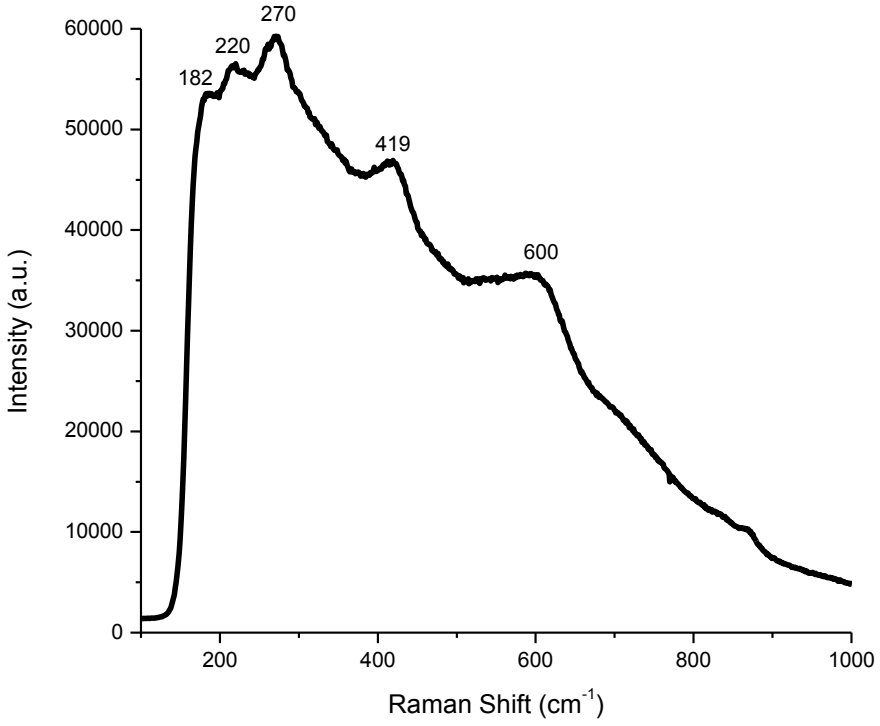

Figure 4.11: Raman spectra of $BaTiO_3$ powders with rGO prepared at 160 °C for 7 hrs.

The Raman spectra of $BaTiO_3$ powders synthesized at temperature 150 °C for 5 and 7 hr reaction time are shown in Figure 4.13. The sample synthesized at 5 hr reaction time presents three strong Raman active modes around 394, 513 and 635 cm^{-1}, and three small sharp modes at 180, 195 and 984 cm^{-1} and three small broad shoulders around 300, 691 and 791 cm^{-1}. It was observed that when the reaction time of $BaTiO_3$ synthesis was increased from 3 hr to 7 hr, the band intensities of modes around 394, 513 and 635 cm^{-1} were decreased (Figure 4.13).

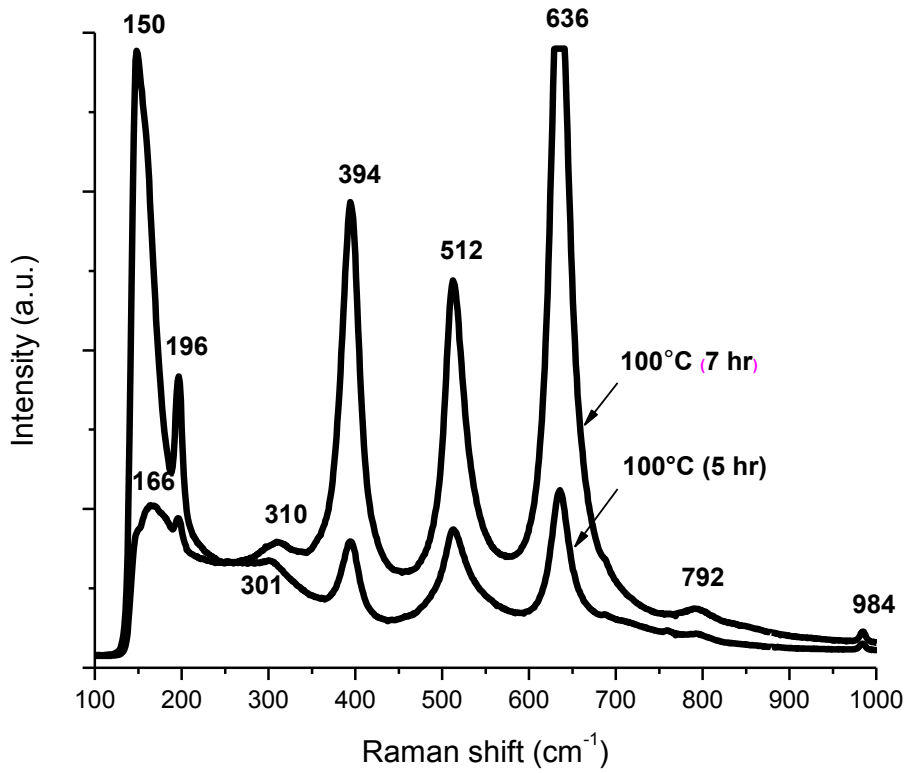

Figure 4.12: Raman spectra of $BaTiO_3$ powders prepared at 100 °C for 5 and 7 hrs.

In addition, the small plasmon peak 180 cm^{-1} present in the 5 hr $BaTiO_3$ powder was disappeared. A sharp band around 160 cm^{-1} and a small broad band at 461cm^{-1} were appeared in $BaTiO_3$ powder synthesized over 7 hr reaction time at 150 °C (Figure 4.13). It was suggested that the peak near 185 cm^{-1} is observed for single-domain single crystals of tetragonal phase $BaTiO_3$ [106]. The low intensity band at 650 cm^{-1} has been suggested to occur in small particle size samples or with a high density of grain boundaries such as in nano-structured polycrystalline films [107]. The appearance of strong Raman peaks near 305 cm^{-1} (B1 mode), that corresponds to tetragonal $BaTiO_3$ phase is contradictory with the cubic symmetry observed by XRD analysis, for which no first-order Raman activity is expected. Busca et al. [108] reported a distortion of the TiO_6 octahedron in the cubic phase $BaTiO_3$ inducing a pseudo-tetragonality of the cubic phase. This could explain the significantly lower symmetry with respect to a cubic perovskite structure, similar to that of tetragonal $BaTiO_3$.

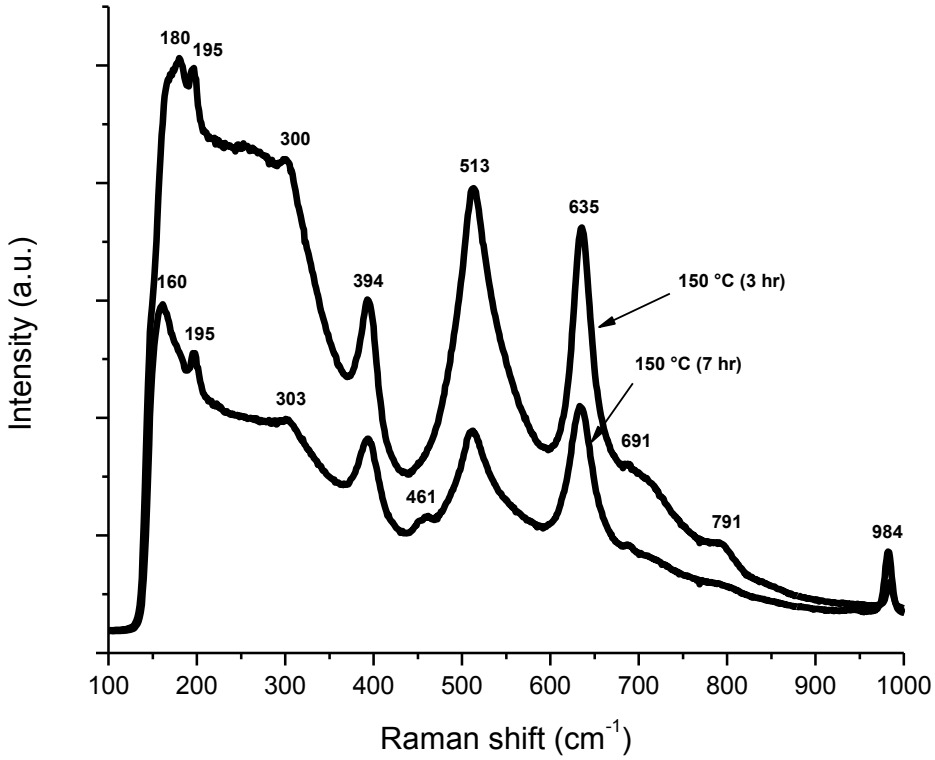

Figure 4.13: Raman spectra of $BaTiO_3$ powders prepared at 150 °C for 5 and 7 hr.

Raman results of $BaTiO_3$ powders prepared at 180 °C for 3 and 7 hr showed strong sharp bands around 160, 393, 512 and 634 cm^{-1}, and two small sharp bands around 198 and 981 cm^{-1} (Figure 4.14). It was observed that the intensities of bands were decreased in sample prepared over 7 hr reaction time at 180 °C. A weak broad plasmon band around 305 cm^{-1} was appeared in both the samples. The frequencies near to 190 and 516 cm^{-1} mode come from the *F*1u cubic phase modes, the 303 cm^{-1} mode comes from the splitting of the cubic silent *F*2u mode [109].

The intensity of the peak around 303 cm-1 was assigned to the overlap of *E*(3TO) + *E*(2LO) + B1, which decreased with an increase in temperature and the mode disappeared above T_c where the structure became cubic.

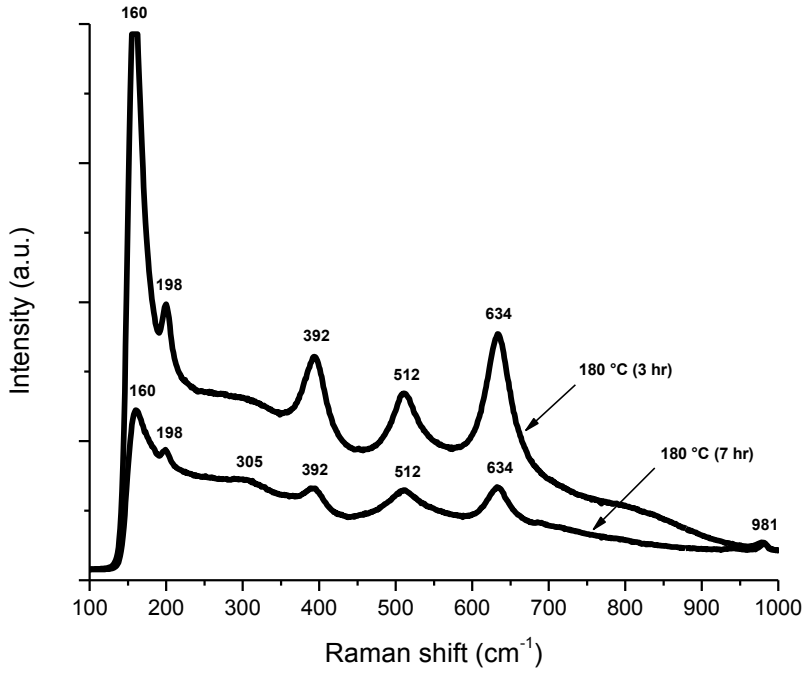

Figure 4.14: Raman spectra of $BaTiO_3$ powders prepared at 180 °C for 3 and 7 hrs.

On comparison, Raman results of $BaTiO_3$ powders prepared at temperatures 100, 150 and 180 °C during 7 hr reaction time are shown in Figure 4.15. The Raman spectra showed the presence of $BaTiO_3$ in these samples. It was observed that the peak intensities were decreased with increase in reaction temperature of synthesis process. Ávila et al. [110] suggested that the peaks at 639, 396 and 144 cm^{-1} correspond to the anatase phase of TiO_2. This observation confirms that the chemical reaction between $Ba(OH)_2$ and TiO_2 was not complete after 7 hr reaction time.

The Raman spectra suggest that the presence of un-reacted TiO_2 was coexisting in all the synthesized $BaTiO_3$ powders (Figure 4.15). However, the concentration of un-reacted TiO_2 corresponding to peak intensities was decreased with increase in reaction temperature during synthesis process. So, it is indicated that less amount of un-reacted TiO_2 was present at higher reaction temperature. Frey and Payne [111] suggested that the positive intensity peak at 193-195 cm^{-1}, which would be indicative of the presence of orthorhombic phase $BaTiO_3$, which is visible in the Raman spectra showing sharp band around 195-198 cm^{-1} in all the $BaTiO_3$ samples. The Raman spectra clearly showed the cubic distortion of $BaTiO_3$ structure coexisted along with un-reacted TiO_2.

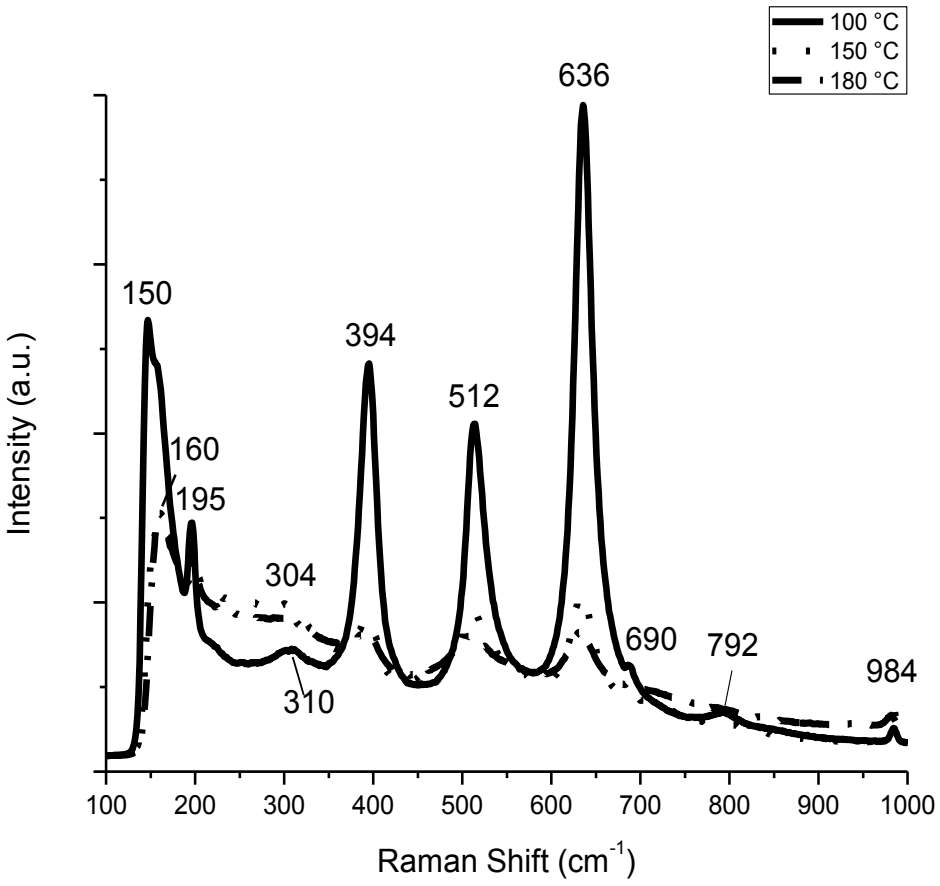

Figure 4.15: Raman spectra of $BaTiO_3$ powders prepared at 100, 150 and 180 °C for 7 hr reaction time.

It is believed that there is a critical crystallite size for the $BaTiO_3$ for stabilizing the cubic or the tetragonal phase [112]. It means that if the crystallite size is lower than the critical value, the phase should be cubic. In the particular case of bulk $BaTiO_3$, the body retains its ferro-electricity unless the average grain size is less than 50 nm [112].

4.2.3. FT-IR Spectroscopy:

FT-IR analysis was carried out for the detection of functional groups present in the synthesized $BaTiO_3$ powders at various reaction temperatures and reaction time. FTIR spectrum of $BaTiO_3$ powder prepared by hydrothermal process at 160 °C for 7 hr reaction time is shown in Figure 4.16. Typical absorption bands found in the FTIR

displayed several types of vibrations at 510, 1080, 1190, 1350, 1380, 1470, 1570, 1980, 2360, 2850 and 3853 cm^{-1}. The absorption band at 1080 cm^{-1} was assigned to the Ti-O stretching. A strong absorption feature at 3565 cm^{-1} has been identified as the stretching mode of OH ions interpreted in the film and is commonly found in pervoskite films grown at low temperature by more conventional techniques.

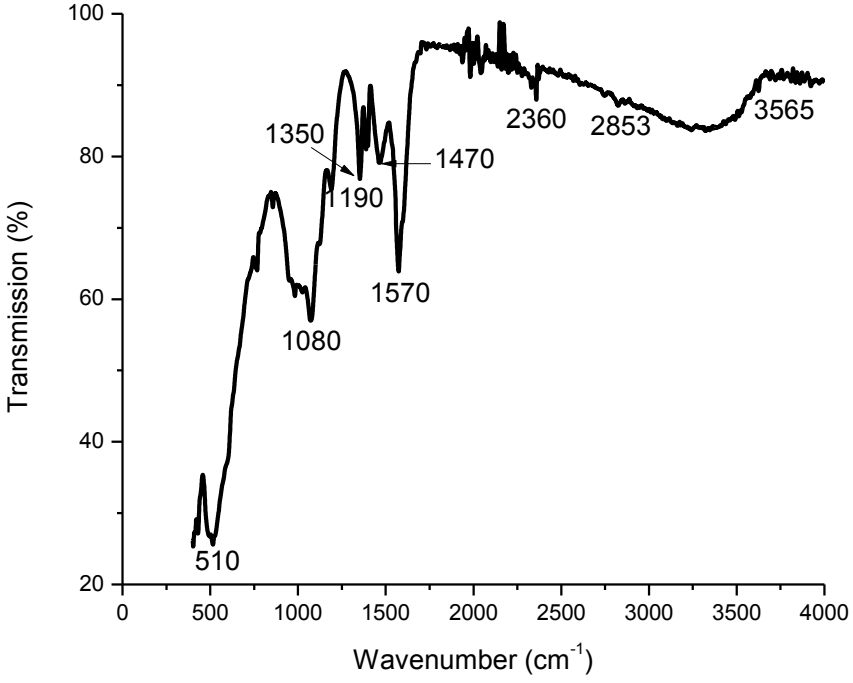

Figure 4.16: FT-IR spectrum of $BaTiO_3$ powder prepared by hydrothermal process carried out at reaction temperature of 160 °C and 7 hr reaction time.

FTIR spectra of $BaTiO_3$ powder samples prepared by hydrothermal process at 100 °C for 5 hr and 7 hr reaction time are shown in Figure 4.17. Typical absorption bands found in the FTIR displayed several types of vibrations at 470, 850, 1080, 1120, 1180, 1350, 1420, 1580, 1750, 2830 and 3565 cm^{-1}. The typical absorption band at 470 cm^{-1} assigned to the 'fingerprint' of $BaTiO_3$ was detected in both the samples [113]. The absorption bands at 1080, 1120, 1180 and 1750 cm^{-1} were assigned to the Ti-O stretching. The characteristic absorption band at 1420 cm^{-1} corresponding to Ba-Ti-O

stretching was detected in both samples. A strong absorption feature at 3565 cm^{-1} has been identified as the stretching mode of OH ions interpreted in the film and is commonly found in pervoskite films grown at low temperature by more conventional techniques. This absorption referred to as hydroxyl defects because of the high mobility of hydrogen in pervoskite materials and is usually annealed out at temperatures near the phase transformation temperatures. Finally, absorption bands at wave number greater than 800 cm^{-1} are related to M-O bands, which are resulted from the Ti-O and Ti-O-Ti bands.

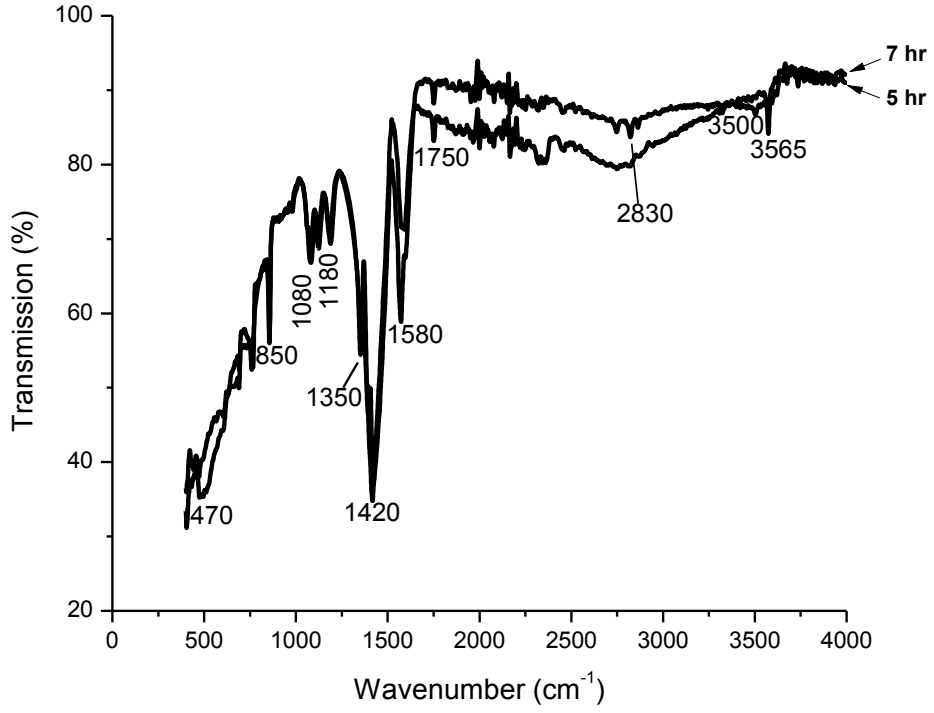

Figure 4.17: FT-IR spectra of $BaTiO_3$ powders synthesized by hydrothermal process at 100 °C for 5 hr and 7 hr reaction time in a stirred autoclave.

FTIR spectra of $BaTiO_3$ powder samples prepared by hydrothermal process at 150 °C for 5 and 7 hr reaction time are shown in Figure 4.18. Typical absorption bands found in the FTIR displayed several types of vibrations at 470, 860, 1080, 1180, 1440, 2360 and 3504 cm^{-1}. The typical absorption band at 470 cm^{-1} assigned to the 'fingerprint' of $BaTiO_3$ was detected in both the samples [113]. The absorption bands at

1080, 1120, 1180 and 1750 cm^{-1} were assigned to the Ti-O stretching. The characteristic absorption band at 1420 cm^{-1} corresponding to Ba-Ti-O stretching was detected in both samples.

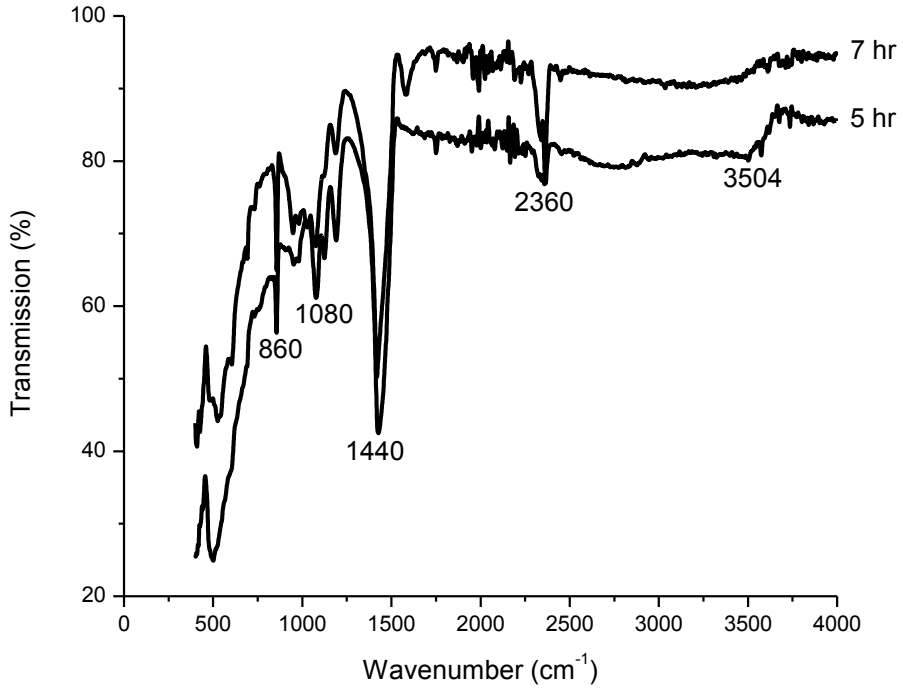

Figure 4.18: FT-IR spectra of $BaTiO_3$ powders synthesized by hydrothermal process at 150 °C for 3hr and 7 hr reaction time in a stirred autoclave.

FTIR spectra of $BaTiO_3$ powder samples prepared by hydrothermal process at 180 °C for 3 hr and 7 hr reaction time are shown in Figure 4.19. Typical absorption bands found in the FTIR displayed several types of vibrations at 470, 540, 850, 950, 1040, 1070, 1190, 1415, 1580, 2170, 2340 and broad peak in the higher frequency range of 3300 cm^{-1}. The broad peak in the lower frequency range, with a center at ~ 550 cm-1, corresponds to stretching vibration in the TiO_6 octahedral [114]. A second peak at lower frequency has been assigned to the Ti-O bending vibration [115]. The weak peak at 2340 cm-1 corresponds to CO_2 adsorbed on a metal cation [116]. The characteristic absorption band at 1420 cm^{-1} corresponding to Ba-Ti-O stretching was detected in both samples. A broad absorption feature at 3300 cm^{-1} has been identified as the stretching mode of OH

ions found in pervoskite films grown at low temperature by more conventional techniques.

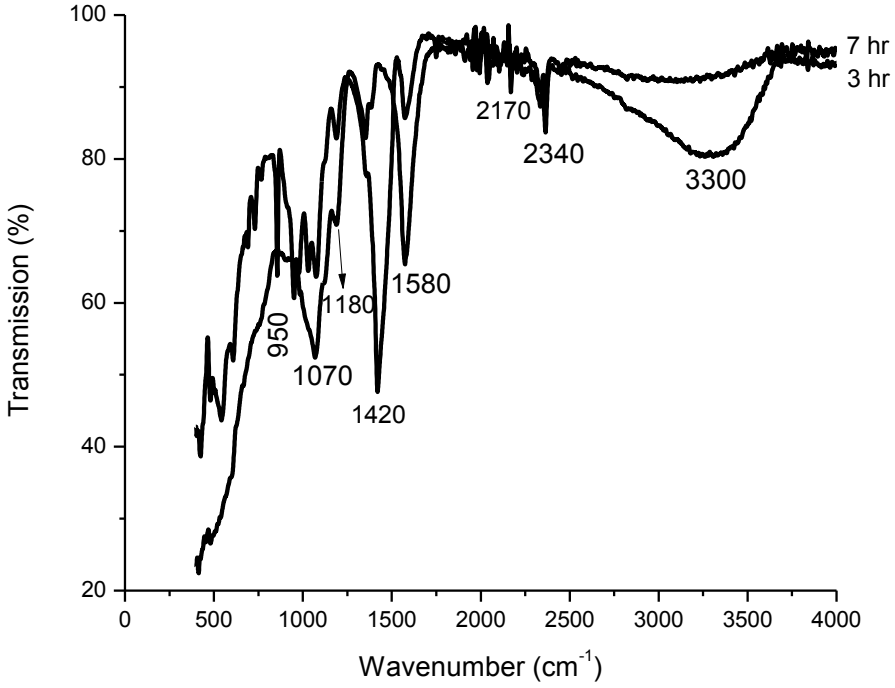

Figure 4.19: FT-IR spectra of $BaTiO_3$ powders synthesized by hydrothermal process at 180 °C for 3hr and 7 hr reaction time in a stirred autoclave.

4.2.4. Scanning electron microscopy:

The primary particle shape and size of the prepared BaTiO3 powders was observed by the scanning electron microscope (SEM). The SEM micrographs of $BaTiO_3$ powder prepared at 100 °C for 7 hr reaction time by hydrothermal process are shown in Figure 4.20. The $BaTiO_3$ particles showed different shapes including irregular, sphere-like, cube-like particles and cube-rod structures. It indicated that the average particle sizes of $BaTiO_3$ powder are 32 nm and 72 nm (Figure 4.20A). The morphological characteristics and size distribution of the prepared powders are shown in Figure 4.20B and 4.20C. It is well known that nanopowders have extremely large specific area and strongly tend to be agglomerated [117]. Therefore, the size estimated from SEM is larger than that calculated from the XRD data.

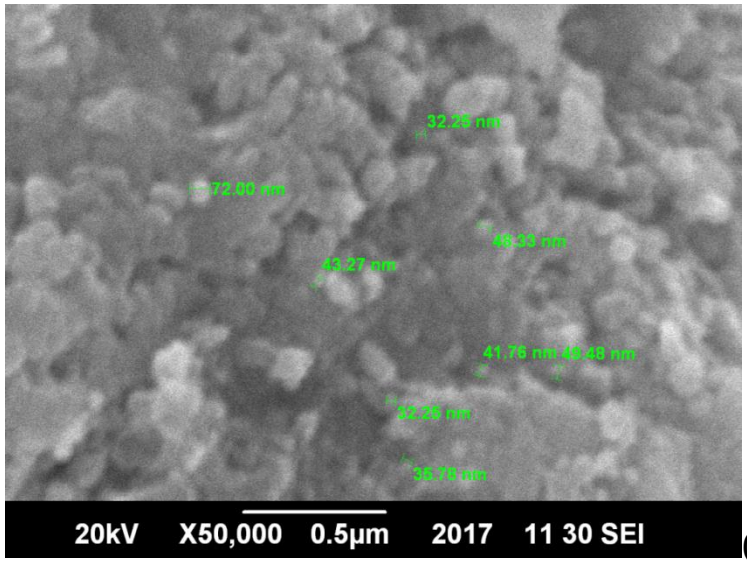

(A)

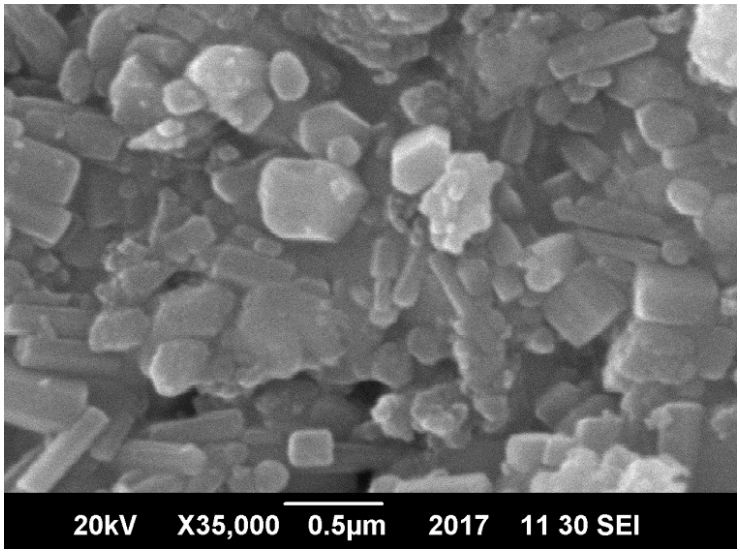

(B)

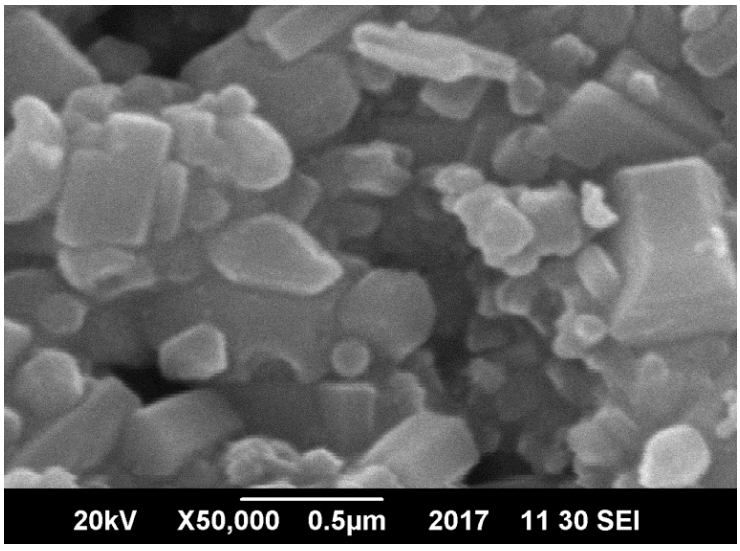

(C)

Figure 4.20: SEM micrographs of $BaTiO_3$ powders prepared by hydrothermal process at 100 °C for 7 hr reaction time in stirred autoclave

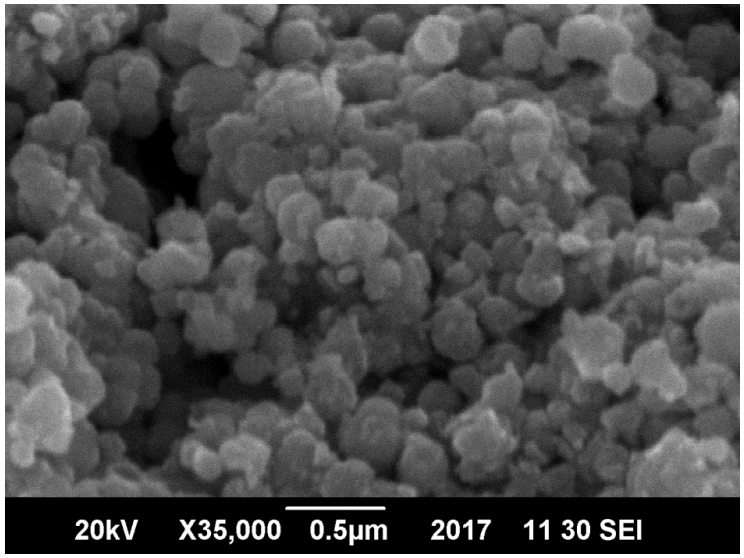

(A)

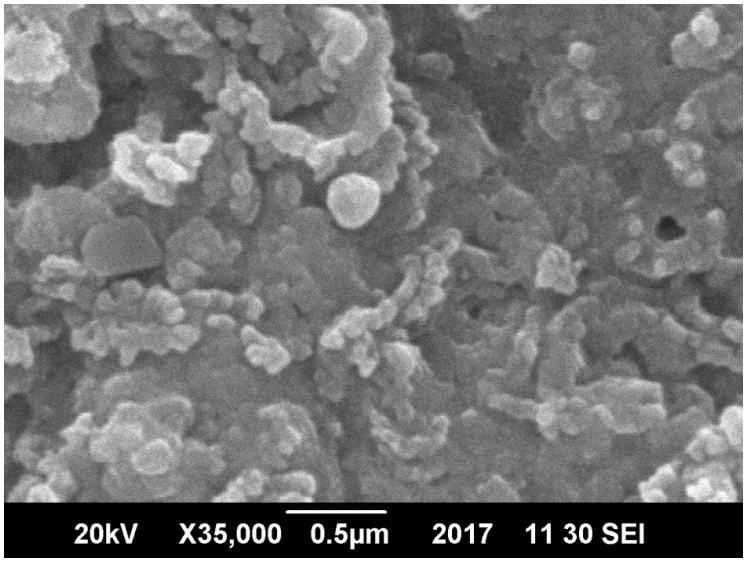

(B)

Figure 4.21: SEM micrographs of $BaTiO_3$ powders prepared by hydrothermal process at 150 °C for 7 hr reaction time in stirred autoclave

The SEM micrographs of $BaTiO_3$ powder prepared at 150 °C for 7 hr reaction time are shown in Figure 4.21. The $BaTiO_3$ particles showed different shapes including irregular and sphere-like and cube structures. The shape and size distribution of the prepared powder showed agglomeration due to nano-sized particles.

The morphological properties of the $BaTiO_3$ prepared at 160 °C for 7 hr indicated irregular, spherical, and cubic structures (Figure 4.22).

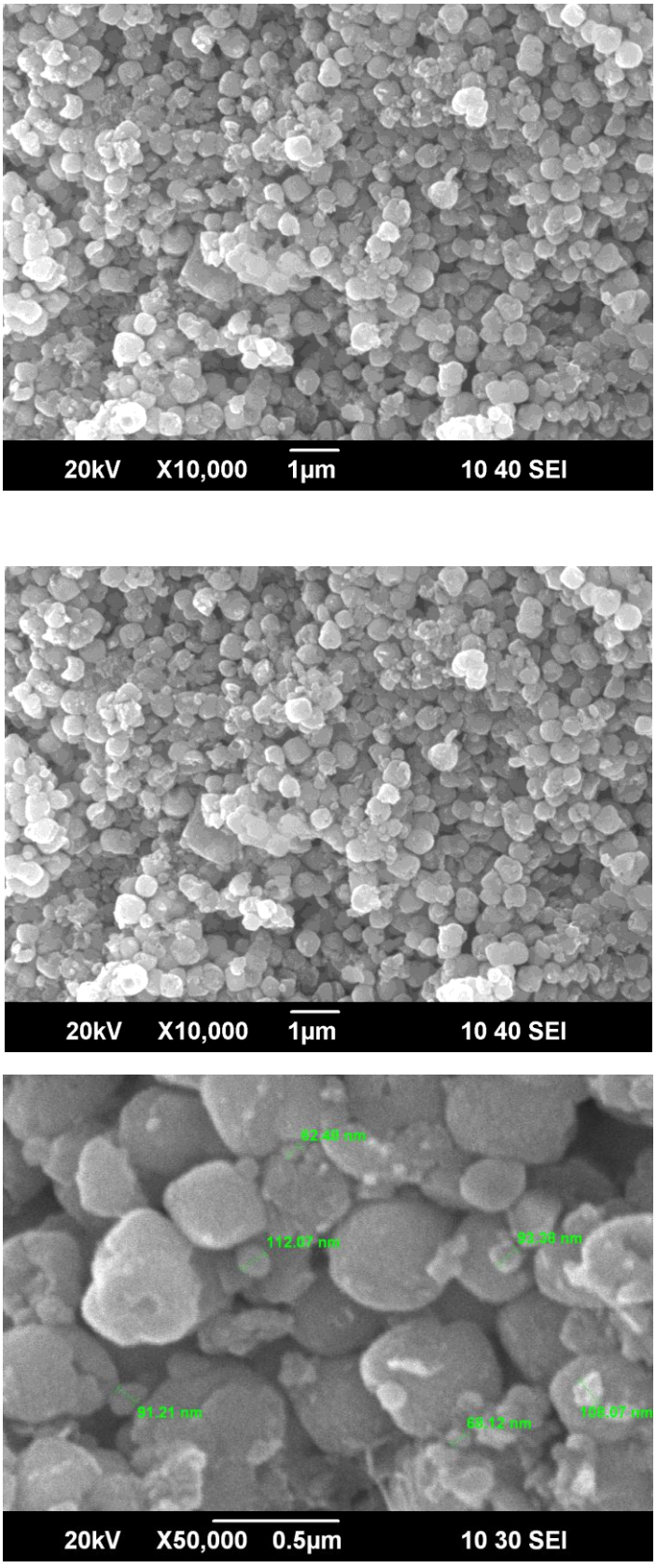

Figure 4.22: SEM micrographs of $BaTiO_3$ powders prepared by hydrothermal process at 160 °C for 7 hr reaction time during hydrothermal process

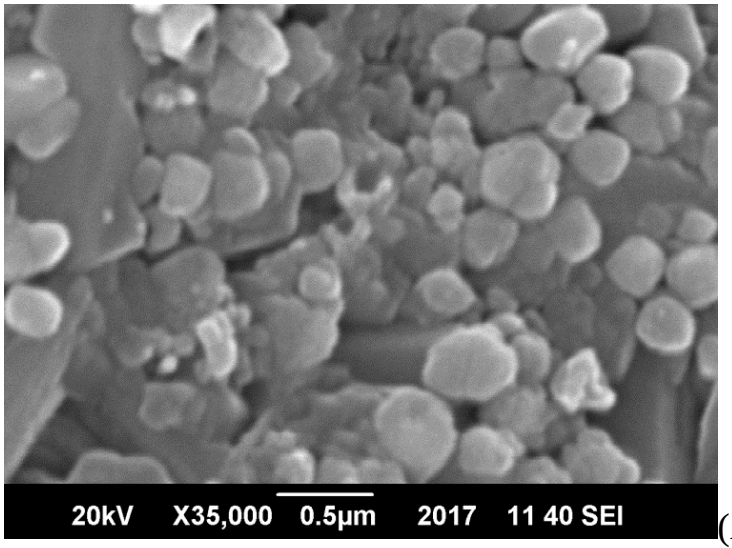

(A)

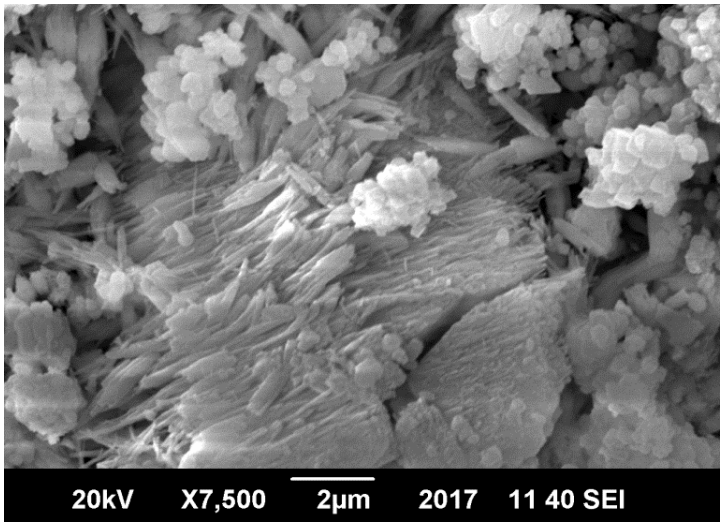

(B)

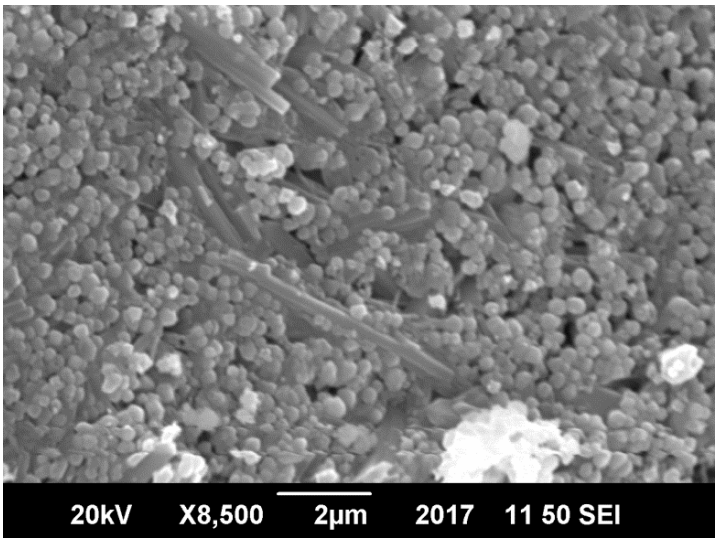

(C)

Figure 4.23: SEM micrographs of $BaTiO_3$ powders prepared by hydrothermal process at 180 °C for 7 hr reaction time during hydrothermal process

The morphological properties of the $BaTiO_3$ prepared at 180 °C for 7 hr clearly indicated irregular, spherical, and rod-like structures (Figure 4.23). Field emission scanning electron micrographs (FE-SEM) of $BaTiO_3$ powders synthesized at 160 °C for 7 hr reaction time in the presence of reduced Graphene Oxide (rGO) during hydrothermal process are shown in Figure 4.24. It is clear that the $BaTiO_3$ particles are cube shape and the shape and size distribution of the prepared powder showed agglomeration due to nano-sized particles.

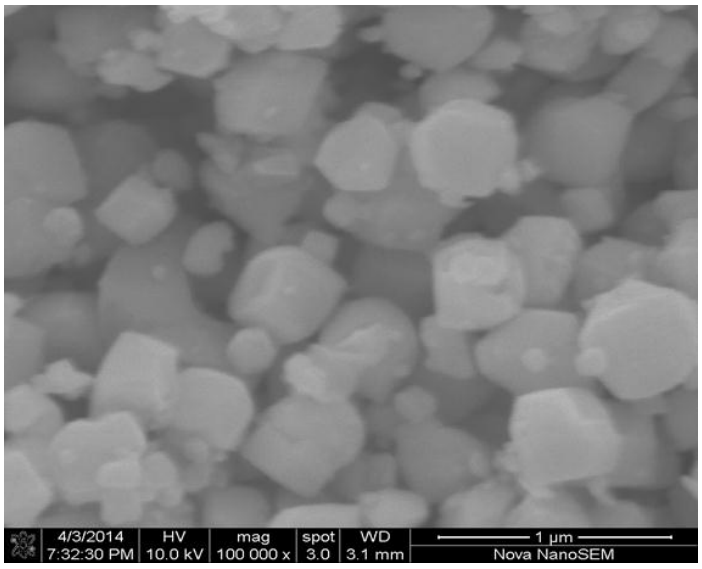

(A)

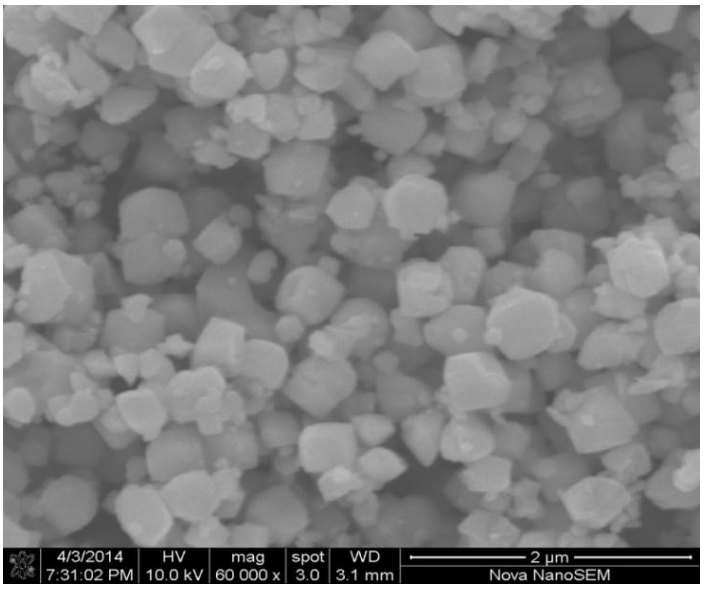

(B)

Figure 4.24: Field emission scanning electron micrographs (FE-SEM) of $BaTiO_3$ powders synthesized at 160 °C for 7 hr reaction time in the presence of reduced graphene oxide (RGO) in stirred autoclave during hydrothermal process.

4.2.5. Impedance Spectroscopy

The impedance analysis of $BaTiO_3$ powder pellets were investigated in the frequency range of 1 KHz to 2 MHz using an Agilent E4980A LCR meter. Impedance spectroscopy data are described in different complex plane formalisms that interrelate and highlight different aspects of the data. Figure 4.25A and Figure 4.25B show the real part of impedance and imaginary part of impedance against frequency of $BaTiO_3$ powders synthesized at different reaction temperature and time by autoclave-assisted hydrothermal reaction. Here the frequency increases from left to right. The data suggest that the resistivity (Z') and loss (Z'') decreases with increase of frequency (Figure 4.25A&B). At low frequency, the data is scattered which might be due to the presence of impurities like $BaCO_3$ and un-reacted TiO_2 in the $BaTiO_3$ powders. All the products were found to be very lossy. The loss is found to be decrease with increase of frequency (Figure 4.25B). The dependence of real against imaginary part of the impedance (Nyquist plots) show that with increase of resistivity of the $BaTiO_3$ powder increase the loss (Figure 4.26).

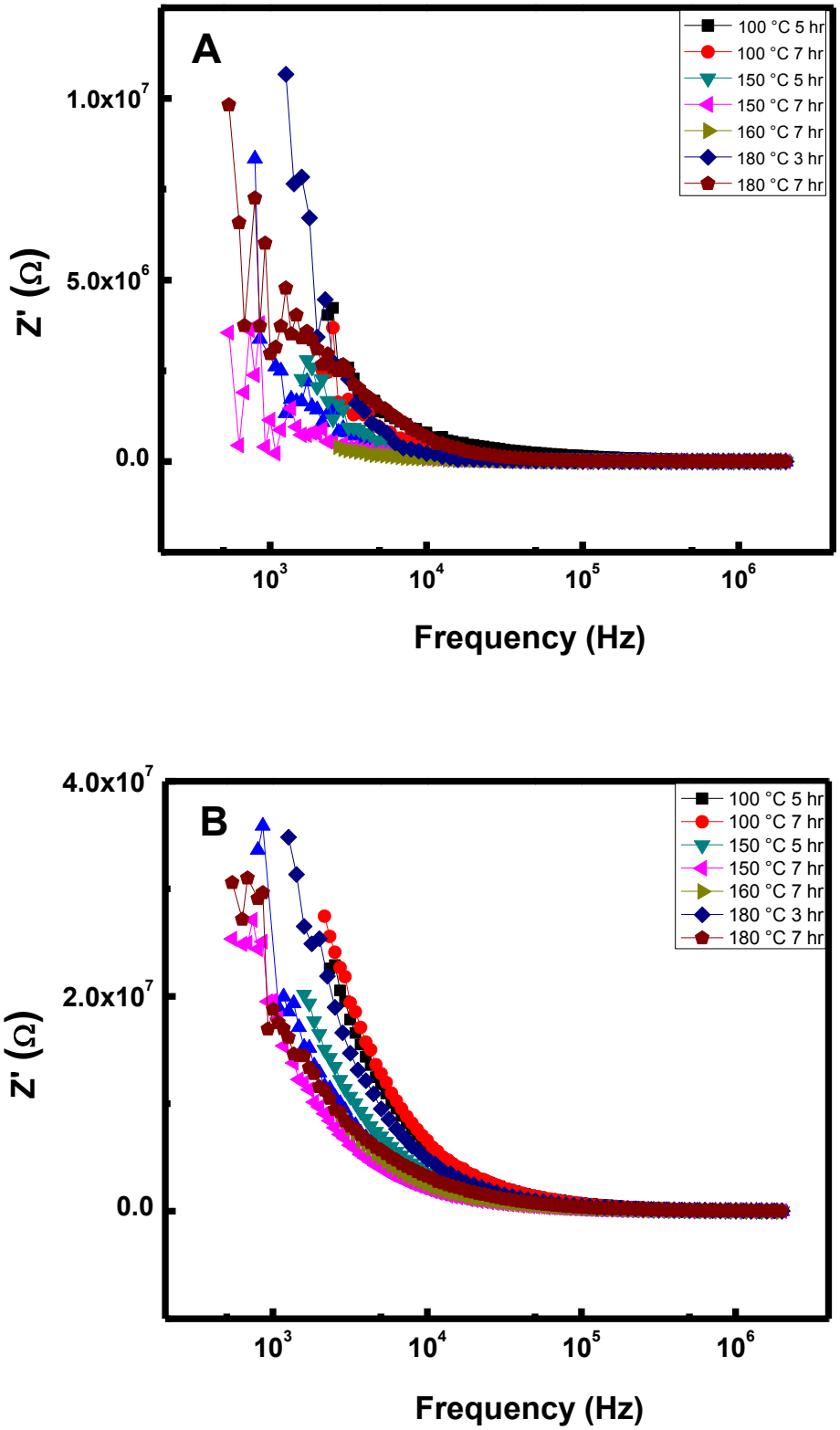

Figure 4.25: (A) Frequency dependent behavior of real part impedance and (B) imaginary part of the impedance of $BaTiO_3$ powders synthesized at different reaction temperature and time.

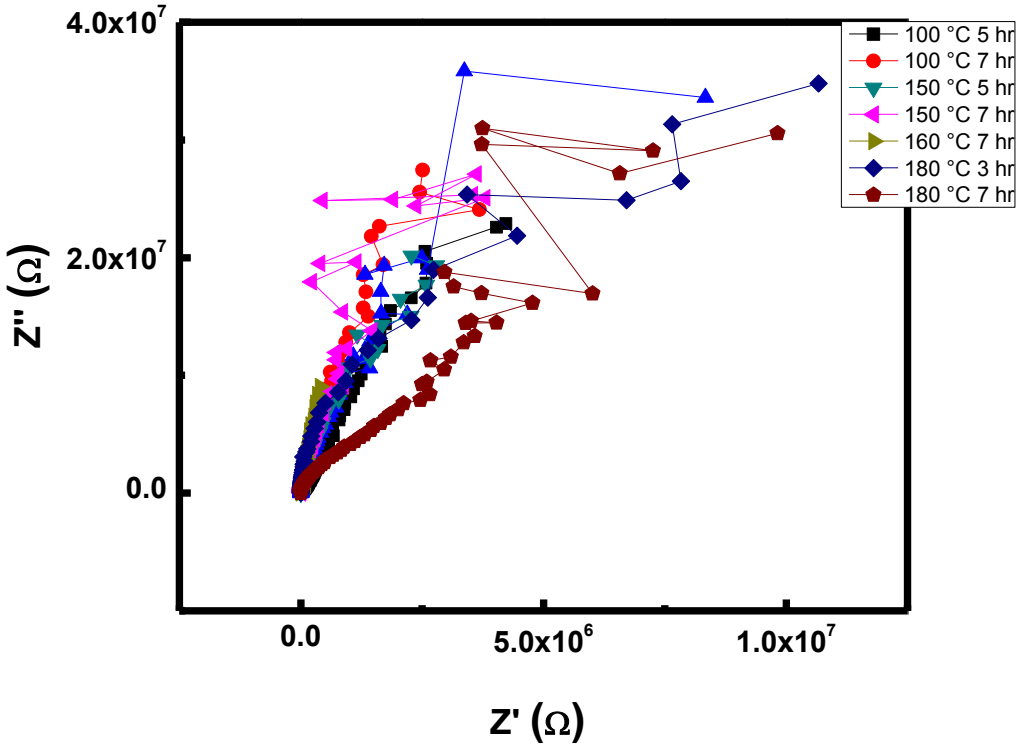

Figure 4.26: Nyquist plots (dependence of real vs imaginary part of the impedance) of $BaTiO_3$ powders synthesized at different reaction temperature and time.

4. Conclusions

Nano-crystallite $BaTiO_3$ powders were successfully synthesized by using $Ba(OH)_2 \cdot 8H_2O$ to TiO_2 at the ratio of [4:1) as a starting materials in stirred reactor by hydrothermal process. The powder samples were characterized by various state-of-the-art techniques viz., X-ray diffraction, SEM, FTIR, Raman and Impedance spectroscopic analyses. XRD data indicate that the $BaTiO_3$ nano-powders are of cubic phase, which is also confirmed by Raman spectroscopy. SEM micrographs show different shapes and fairly narrow size of distribution of particles. The shape and size of $BaTiO_3$ is affected with reaction temperature and time during hydrothermal synthesis process. The formation of $BaCO_3$ and residual TiO_2 phases as impurities were detected in the $BaTiO_3$ powders in almost all the samples except the powder produced at 160 °C and 7 hr reaction time in the presence of reduced graphene oxide (rGO).

References

[1] Q. Feng, M. Hirasawa, K. Yanagisawa, Chem. Mater. 13 (2001) 290

[2] W.L. Suchanek., R.E. Rimen, Adv. Sci. Technol. 45 (2006) 184

[3] K. Byrappa, in: Kirke-Othmer Encyclopedia of Chemical Technology, John Wiley and Sons, London, 2005

[4] M. Yoshimura, W. Suchanek, K. Byrappa, Mater. Res. Soc. Bull. 25 (2000) 17

[6] S. Stupp, P.V. Braun, Science 277 (1997) 1242

[7] S. Venigalla, Am. Ceram Soc. Bull. 6 (2001) 6

[8] H.A. Âvila, L.A. Ramajo, M.M. Reboredo, et al., Ceramics International 37 (2011) 2383

[9] S. Aoyagi, Y. Kuroiwa, A. Sawada, et al., J. Therm. Anal. Calorim. 81 (2005) 627

[10] R. Roy, J. Solid State Chem., 111 (1994) 11

[11] S. Komameni, R. Roy, Q, H. Li, Mater. Res. Bull., 27 (1992) 1393

[12] W. Suchanek, M. Yoshimura, J. Am. Ceram. Soc., 81 (1998) 2864

[13] M. Yoshimura, W. Suchanek, Solid State Ionics, 98 (1997) 197-208

[14] J.A. Switzer, C.J. Hung, B.E. Breyfogle, et al., Science, 264 (1994) 1573

[15] I. Villegas, J.L. Stickney, J. Electrochem. Soc. 139 (1992) 686

[16] L.P. Colletti, B.H. Flowers Jr., J.L. Stickney, J. Electrochem. Soc. 145 (1998) 1442

[17] G.W. Morey, J. Arnor. Ceram. Soc. 36 (1953) 279

[18] L. Xue, Y. Yan, J. Nanosci. Nanotech. 10 (2010) 973

[19] B. Bhusan (Ed.), Handbook of Nanotechnology, Springer-Verlag, Germany, 2004

[20] M. Rajamathi, R. Seshadri. Curr. Opin. Solid State Mater. 6 (2002) 337

[21] C. Burds, X. Chen, R. Narayanan, M.A. Al-Sayed, Chem. Rev., 105 (2005) 1025

[22] B. Jancar, D. Suvorov, Nanotechnology, 17 (2006) 25

[23] P. Gao, Y. Xie, Y, Chen, L. Ye, Q. Guo, J. Cryst. Growth, 285 (2005) 555

[24] H.S. Qian, S.-H. Yu, J.-Y. Gong, et al., Langmuir, 22 (2006) 3830

[25] G.P. Patzke, F. Krumeich, R. Nesper, Agnew. Chem. 114 (2002) 2554

[26] Z.G. Shen, J.F. Chen, et al, J. Colloid. Interface Sci. 275 (2004) 158

[27] S. Ijima, Nature 354 (1991) 56

[28] A. Testino, M.T. Buscaglia, et al, Chem. Mater. 16 (2004) 1536

[29] A.D. Hilton, R. Forst, Key Eng. Mater. 66-67 (1992) 145

[30] J.O. Eckert, C.G. Hung-Houston, B.L. Gersten, et al., J. Am. Ceram. Soc. 79 (1996) 2929

[31] H. Kumazawa, S. Anne, E. Soda, J. Mater. Soc. (1995) 30

[32] L.K. Templeton, J.A. Pask, J. Am. Ceram. Soc. 42 (1959) 212

[33] A. Beauger, J.C. Mutin, J.C. Niepce, J. Mater. Sci. 18 (1983) 3543

[34] A. Kareiva, S. Tautkus, R. Rapalaviciute, et al., J. Mater. Sci. 34 (1999) 4853

[35] H.S. Potdar, S.B. Deshpande, et al., Mater. Chem. Phys. 58 (1999) 121

[36] B.L. Newalkara, S. Komarneni, et al., Mater. Res. Bull. 36 (2001) 2347

[37] R. Ueyama, M. Harada, et al., J. Mater. Sci. 11 (2000) 139

[38] P. Pinceloup, C. Courtois, J. Vicens, et al., J. Eur. Ceram. Soc. 19 (1999) 973

[39] A. Testino, V. Buscaglia, M.T. Buscaglia, et al., Chem. Mater. 17 (2005) 5346

[40] A. Habib, in: Hydrothermal Synthesis of Nanocrystalline Barium Titanate and the Production of thin Ceramic-Polymer Dielectric Films. Ph.D. Dissertation, Vienna University of Technology, July 2008

[41] L.L. Hench, L.K. West, Principles of Electronic Ceramics, John Wiley & Sons, Inc., (1990) pp 244-247

[42] B. Jaffe, W.R. Cook, Jr., H. Jaffe, in: Piezoelectric Ceramics, Academic Press Limited, (1971), pp 50

[43] K. Byrappa, in: Kirke Othmer Encyclopedia of Chemical Technology, John Wiley and Sons, London, 2005

[44] http://cst-www.nrl.navy.mil/lattice/struk/perovskite.html

[45] Yoon, D.-H., B.I. Lee, J. Ceram. Proc. Res. 3 (2002) 41

[46] D.S. Seo, J.K. Lee, H. Kim, J. Cryst. Growth 229 (2001) 428

[47] Clarke, R., J. Appl. Crystall. 9 (1976) 335

[48] W.J. Merz, Physical Rev. 76 (1949) 1221

[49] K. Uchino, E. Sadanaga, T. Hirose, J. Am. Ceram. Soc. 72 (1989) 1555

[50] K. Kinoshita, A. Yamaji, J. Appl. Phys. 47 (1976) 371

[51] P.P. Phule, S.H. Risbud, J. Mater. Sci. 25 (1990) 1169

[52] F. Chaput, J.-P. Boilot, A. Beauger, J. Am. Ceram. Soc. 73 (1990) 942

[53] A.T. Chien, J.S. Speck, F.F. Lange, et al., J. Mater. Res. 10 (1995) 1784

[54] J.G. Eckert, Jr., C.C. Hung-Houston, et al., J. Am. Ceram. Soc. 79 (1996) 2929

[55] L. Zhao, A.T. Chein, F.F. Lange, et al., J. Mater. Res. 11 (1996) 1325

[56] Y-S. Her, E. Matijevic, J. Mater. Sci. 10 (1995) 3106

[57] M.M. Lencka, R.E. Riman, Chem. Mater. 5 (1993) 61

[58] J. Moon, E. Suvaci, T. Li, et al., J. Eur. Ceram. Soc. 22 (2002) 809

[59] C. Pithan, D. Hennings, et al., J. Appl. Ceram. Technol. 2 (2005) 1
[60] C.G. Yanez, C. Benitez, et al., Ceram. Int. 26 (2000) 271
[61] Y. Mao, S. et al., Chem. Commun. (2003) 408
[62] A. Kareiva, S. Tautkus, R. Rapalaviciute, et al., J. Mater. Sci. 34 (1999) 48535
[63] J.J. Urban, W.S. Yun, Q. Gu, H. Park, J. Am. Ceram. Soc. 124 (7) (2002) 1186
[64] I.J. Clark, T. Takeuchi, N. Ohtori, D.C. Sinclair, J. Mater. Chem. 9 (1999) 83
[65] M. Hu, V. Kurian, E.A. Payzant, et al., Powder Technol. 110 (2000) 2
[66] P.P. Phule, S.H. Risbud, J. Mater. Sci. 25 (1990) 1169
[67] A.T. Chien, J. Speck, S. Lange, et al., J. Mater. Res. 10 1995) 1784
[68] M. M. Lencka and R. E. Riman, Chem. Mater. 5 (1993) 61
[69] M. M. Lencka and R. E. Riman, Ferroelectrics, 151 (1994) 159
[70] L. Mazzola, Nat. Mater. 4 (2005) 575
[71] C.C. Tsai, H. Teng, Chem. Mater. 16 (2004) 4352
[72] T. Qui, X.L. Wu, Y.F. Mei, et al., J. Cryst. Growth 277 (2005) 143
[73] D. Wang, D. Yu, Y. Peng, et al., Nanotechnology 14 (2003) 748
[74] S. Wada, T. Suzzuki, T. Noma, J. Ceram. Soc. Jpn. 103(1995) 1220
[75] D-H. Yoon, B.I. Lee J. Eur. Ceramic Soc. 24 (2004) 753
[76] X. Zhu, J. Zhu, S. Zhou, et al., J. Crystal Growth 283 (2005) 553
[77] T. Yan, X.L. Liu, N.R. Wang, J.F. Chen, J. Cryst. Growth 281 (2005) 669
[78] P.K. Dutta, J.R. Gregg, Chem. Mater. 4 (1992) 843
[79] S. Wada, H. Chikamori, T. Noma, T. Suzuki, J. Mater. Sci. Letts. 9 (2000) 245
[80] W. Hertl, J. Am. Ceramic Soc. 71 (1988) 879
[81] E. Ciftci, M.N. Rahaman, M. Shumsky, J. Mater. Sci. 36 (2001) 4875
[82] L. Qi, B. I. Lee, et al., J. Eur. Ceram. Soc. 24 (2004) 3553
[83] T. Chaiyot, Powder Technol. 124 (2002) 67
[84] Y. Zeng, D. Jiang, G. Peter, J. Eur. Ceram. Soc. 20 (2000) 1691
[85] N.A. Ovramenko, et al., Neorg. Mater.15 (1979) 1982
[86] P. Pinceloup, C. Courtois, J. Vicens, et al., J. Eur. Ceram. Soc. 19 (1999) 973
[87] I. MacLaren, C.B. Ponton, J. Eur. Ceram. Soc. 20 (2000) 1267
[88] P.K. Dutta, R. Asiaie, S.A. Akbar, W. Zhu, Chem. Mater. 6 (1994) 1542
[89] Y. Ma, E. Vileno, S.L. Suib, P.K. Dutta, Chem. Mater. 9 (1997) 3023
[90] M. Wu, J. Long, et al., J. Am. Ceram. Soc., 82 (1999) 3254
[91] H. Xu, L. Gao, J. Guo, J. Eur. Ceram. Soc., 22 (2002) 1163

[92] Q. Feng, M. Hirasawa, K. Yanagisawa, Chem. Mater. 13 (2001) 290

[93] R.E. Riman, W.L. Suchanek, M.M. Lencka, Ann. Chim. Sci. Mat. 27 (2002) 15

[94] I.A.Aksay, C.M. Chun, et al, in: Proc. 2nd Inter. Conf. Solvotherm. Reactions, Takamatsu, Japan, Dec. 18–20, 1996, pp. 76

[95] M. Zeng, Appl. Surface Sci. 257 (2011) 6636

[96] H.A. Âvila, L.A. Ramajo, et al, Ceramics International 37 (2011) 2383

[97] J. Moon, E. Suvaci, A. Morrone, et al., J. Eur. Ceram. Soc. 23 (2003) 2153

[98] Y.S. Her, E. Matijevif, M.C. Chon, J. Mater. Res. 10 (1995) 3106

[99] M. Leoni, M. Viviani, P. Nanni, V. Buscaglia, J. Mater. Sci. Lett. 15 (1996) 1302

[100] R. Vijayalakshmi, V. Rajendran, Digest J. Nanomater. Biostructures, 5 (2010) 511

[101] G. Busca, V. Buscaglia, M. Leoni, P. Nanni, Chem. Mater. 6(1994) 955

[102] S.W. Lu, B.I. Lee, Z.I. Wang, W.D. Samuels, J. Cryst. Growth, 219 (2000) 269

[103] M. Boulos, S. Guillemet-Fritsch, et al., Solid State Ionics 176 (2005) 301

[104] D. Teme, X. Xi. J. Am. Ceram. Soc. 91 (2008) 1820

[105] S. Fuentes, R.A. Zárate, et al, J. Alloys Compd. 505 (2010) 568

[106] M.H. Frey, D.A. Payne, Phy. Rev. B 54 (1996) 3158

[107] V. Buscaglia, M. T. Buscaglia, et al, J. Eur. Ceram. Soc. 25 (2005) 3059

[108] G. Busca, V. Buscaglia, M. Leoni, P. Nannit, Chem. Mater. 6 (1994) 955

[109] Z. Lazarević, N. Romćević, et al, 2008, Proc. 3rd Annual Conf. Materials Res. Soc. Serbia, Sept. 2008, 808

[110] H.A. Ávila, L.A. Ramajo, et al, Ceram. Int. 37 (2011) 2383

[111] M.H. Frey, D.A. Payne, Phy. Rev. B 54 (1996) 3158

[112] A. Sundaresan, R. Bhargavi, et al, Phy. Rev. B 74 (2006) 161306

[113] C.-T. Xia et al., Journal of Crystal Growth 166 (1996) 961-966222

[114] K.S. Mazdiyasni, R.T. Dollof, J.S. Smith, J. Am. Ceram. Soc. 52 (1969) 523

[115] J.T. Last, Phy. Rev. 105 (1957) 1740

[116] A. Lercher, C. Colombier, et al, J. Chem. Soc. Faraday Trans. 1, 80 (1984) 949.

[117] X.Y. Wang, B. Lee, et al, J. Eur. Ceram. Soc. 26 (2006) 2319.